Structural controls on the emplacement and evacuation of magma from a sub-volcanic laccolith; Reyðarártindur Laccolith, SE Iceland

Vincent Twomey[1]†, William McCarthy[1], Craig Magee[2]

1 School of Earth & Environmental Sciences, University of St Andrews, St Andrews, UK, KY16 9AL.

2 School of Earth and Environment, University of Leeds, Leeds, UK, LS2 9JT

†Corresponding author: email: vt22@st-andrews.ac.uk

Abstract

Laccoliths play a significant role in the transport and storage of magma in sub-volcanic systems. Yet controls on laccolith construction, which influence the location and form of magma evacuation conduits that potentially feed volcanic eruptions, remains poorly documented in natural examples. The excellently exposed sub-volcanic Miocene Reyðarártindur Laccolith in SE Iceland provides an opportunity to investigate the mechanisms that control on magma emplacement and evacuation during laccolith construction. Detailed structural mapping combined with anisotropy of magnetic susceptibility (AMS) analyses show that the laccolith comprises of several laterally intruded magma lobes that inflated and coalesced along a NE-SW primary axis, facilitated by forced folding of the host rock. NNE-striking, left-stepping, en-echelon fault/fractures facilitate moderately to steeply inclined rhyolitic/granophyric sheets that emanate outward from the lateral terminations of some flow lobes where, magnetic foliations suggest that magma evacuated upward along these sheets. Thus, potential eruptions these sheets may have fed would have been laterally offset from the laccolith and overlying intrusion-induced surface deformation. Our study shows that magma evacuation and ascent from laccoliths can be facilitated by inclined sheets that form at the lateral terminations of magma lobes that are spatially controlled by laccolith construction and the presence of pre-existing structures.

Supplementary material: Complete structural analysis tables (SiroVision), Thermomagnetic experiment tables with sample localities, AMS Plot map and, Petrography are available at:

The construction of sub-volcanic magma plumbing systems, of which laccoliths are often key components, controls the location of volcanoes and the host rock deformation patterns used to track and monitor potential eruptions (e.g., Johnson and Pollard, 1973; Pollard *et al.* 1975; Rocchi *et al.* 2002; Morgan *et al.* 2008; Sparks *et al*. 2012; Castro *et al.* 2016). Numerous studies demonstrate that laccolith construction commonly occurs through lateral emplacement of incrementally assembled magma pulses, with space generated by deformation of the surrounding host rock (e.g., Pollard *et al.* 1975; Koch *et al*. 1981; Thomson, 2007; Stevenson *et al.* 2007a; Menand 2008; Michel *et al.* 2008; Magee *et al.* 2012a; Roni *et al*. 2014; Wilson *et al.* 2016; Horsman *et al.* 2018; Galland *et al.* 2018). The evacuation of magma from these laterally injected magma pulses, and the laccoliths they form, is typically interpreted to occur via either vertical conduits that overlie the intrusion (e.g., Castro *et al.* 2016) or by inclined sheets that emanate from outer intrusion tips (e.g., Thomson 2007; Wilson *et al.* 2016). However, the processes that influence laccolith construction leads to the formation of these conduits and how magma reacts to their formation is poorly understood.

The excellent 3D exposure of the Reyðarártindur Laccolith, one of a suite of silicic to composite sub-volcanic intrusions in SE Iceland (Fig. 1), provides a superb natural laboratory to investigate the mechanisms of laccolith construction and their control on magma evacuation. In this paper, we combine anisotropy of magnetic susceptibility (AMS) data from both the Reyðarártindur Laccolith and inclined sheets around the intrusion periphery, with detailed structural analysis of the surrounding host rock to unravel the controls on magma emplacement dynamics. By integrating magma flow parameters with observed host-rock structures we have created a new model demonstrating the structures that control the manner and location of magma ascent from a sub-volcanic laccolith to potential eruption sites. Our results offer new insights on the structural controls of magma flow in sub-volcanic plumbing systems and the subsequent impact on eruption location and intrusion-induced surface deformation patterns that are critical to volcanic hazard assessment.

Geological setting

The geology of Iceland is dominated by comprises primarily of gently tilted, layered basaltic lava piles which forms part of the oceanic lithosphere that has been elevated above sea level due to extensive magmatism emanating from the interaction of the Mid-Atlantic Ridge with a deep-rooted mantle plume (e.g., Schilling 1973; Walker 1974; Saemundsson 1980; Sigmundsson *et al.* 2018). Exposures of abandoned ~15–2 Ma oceanic rift segments within the lavas are characterised by sub-parallel swarms of NNW-SSW tension fractures, normal faults, dykes, and eruptive fissures that indicate a WNW-ESE extensional direction (Fig. 1; Saemundsson 1980; Thorarinsson and Tegner 2009; Burchardt *et al.* 2012a; Hjartardóttir *et al.* 2012; Weismüller *et al.* 2019). Lava piles dip gently towards these ancient rift segments, and the current rift axis, as continued burial of older lava flows by newly extruded material causes their subsidence and horizontal axis rotation in the direction of the rift (Bodvarsson and Walker 1964). Burial of the flood basalts under high geothermal gradients leads to localised partial melting, which produces mafic, silicic, and mixed melts in the upper crust (Pálmason 2015). The transport and emplacement of these melts through the layered basaltic pile is channelled into discrete plumbing systems at <1.0–4.7 km depths that likely form the roots of central volcanoes (Klausen 2004, 2006; Eriksson *et al.* 2011; Padilla *et al.* 2016; Sturkell *et al.* 2003, 2006; Alfaro *et al.* 2007; Mattsson *et al.* 2018).

In SE Iceland, the ~15 km^2, ~350 m thick, Reyðarártindur Laccolith and adjacent inclined sheet intrusions, exposed due to Plio-Pleistocene glaciations, are interpreted to belong to a suite of coeval composite to silicic plutonic complexes that likely represent the plumbing system of the Miocene-Pliocene Lon Central Volcano (Figs 1 & 2; (Burchardt *et al.* 2012a),(Burchardt *et al.* 2012a, b). These intrusions are inferred to be derived from melting of hydrated metabasaltic crust in rift zones, followed by assimilation and/or fractional crystallization (Martin and Sigmarsson 2010; Padilla *et al.* 2016). The Reyðarártindur Laccolith comprises of zones of granophyre, granite/granodiorite, and a composite mafic-felsic “net-veined complex” (e.g., Fig. 2; Mattson *et al.* 1986; Furman *et al.* 1992). The laccolith is interpreted to have been emplaced at a depth of ~1.0 km below the surface based on the distribution of zeolite facies metamorphism in the surrounding fine-grained, aphyric host lavas (Walker 1974). The laccolith and flood basalts were subsequently tilted by up to 8–10° to the northwest from continuous loading of the flood basalt by younger basaltic magma derived from the active rift zone to the west, (Fig. 1; Walker 1974; Saemundsson 1980; Gudmundsson 2012).

Methods

Lithological and structural mapping of the laccolith and surrounding host rock were conducted using the FieldMOVE^{TM} application (https://www.mve.com/digital-mapping/) with an iPad tablet. Structural data such as fault, fracture, contact and host rock orientation were measured with FieldMOVE^{TM} digital compass and regularly validated with an analog compass.

Unmanned aerial vehicle (UAV) photogrammetry

Unmanned aerial vehicle (UAV) photogrammetry acquires geospatially referenced, overlapping digital aerial images, from which Structure from Motion (SfM) algorithms can generate spatial 3D datasets (e.g., Bemis *et al.* 2014; Vollgger and Cruden 2016). UAV photogrammetry was applied to map the geometry of the laccolith boundary and characterise its surrounding host rock structure (i.e., fault and fracture patterns), allowing us to relate deformation features to emplacement. The aerial imagery was acquired using a DJI Phantom III Professional drone (quadcopter) mounted with a 12.4 Mega Pixel digital camera facing directly downwards on a 3-axis gimbal. The flight patterns were set in and around the structural aureole at altitudes ranging between 40-60 meters AGL and with a 70% overlap of geospatially referenced images. A 3D point cloud model and Digital Elevation Model (DEM) were created using Pix4Dmapper Pro software which applied SfM photogrammetry to process the raw aerial imagery. The dataset was subsequently imported into the SiroVision 6.2 photogrammetry program, where the orientations of planar surfaces (e.g., faults, joints, surfaces of layered basalts) were manually traced from the 3D surface models. Circular histograms (rose plots) of identified discontinuities were then plotted on a lower hemisphere stereographic projection.

Anisotropy of magnetic susceptibility

Anisotropy of magnetic susceptibility (AMS) allows the rapid and precise measurement of magnetic fabrics from large sample sets (Tarling and Hrouda 1993). It is well established that magnetic lineations and foliations, particularly those reflecting the shape, orientation, and distribution of ferromagnetic minerals (e.g., magnetite), can record primary magma flow patterns in igneous bodies (e.g., Knight and Walker 1988; Archanjo *et al.* 1995; de Saint-Blanquat *et al.* 2006; Stevenson *et al.* 2007a, b; Petronis and O'Driscoll 2013; McCarthy *et al*. 2015a, b) and smaller sheet intrusions (Cañón-tapia and Chávez-Álvarez 2004; Féménias *et al.* 2004; Philpotts and Philpotts 2007; Petronis *et al*. 2013; Magee *et al.* 2016). For example, discrete magma lobes have been interpreted within some plutons following recognition of narrow zones comprising parallel fabrics that diverge outwards along-strike and then curve inwards to define bulbous terminations (e.g., Cruden *et al.* 1999; Stevenson *et al.* 2007a; Magee *et al.* 2012b). Similarly, increasing velocity gradients adjacent to sheet margins can cause the rotation and imbrication of crystals during magma flow, which can be measured using AMS and related to the magma flow direction; i.e. the intersection point of imbricated fabrics is considered to be orthogonal to the flow direction (e.g., Knight and Walker 1988; Tauxe 1998; Callot *et al.* 2001; Geoffroy *et al.* 2002, 2007; Féménias *et al.* 2004; Eriksson *et al.* 2011, 2015; Porreca *et al.* 2015).

AMS analysis involves the measurement of the bulk magnetic susceptibility of an individual sample along multiple axes to determine a 3D susceptibility tensor defined by three orthogonal principal axes ($K_1 \geq K_2 \geq K_3$) (Robertson 1985). The maximum axis (K_1) usually defines the magnetic lineation, which is typically parallel to the crystallographic long axis of crystals (Tarling and Hrouda, 1993). The short axis (K_3) commonly defines the pole to the magnetic foliation plane (i.e., the K_1-K_2 plane). The size (K_m), shape (T_j), and strength (or ellipticity; P_j) of the ellipsoid is quantified using the following parameters:

$$Km = (K_1 + K_2 + K_3)/3$$

$$P_j = \exp\sqrt{2[(\eta_1 - \eta_m)^2 + (\eta_2 - \eta_m)^2 + (\eta_3 - \eta_m)^2]}$$

$$T_j = \frac{2\eta_2 - \eta_1 - \eta_3}{\eta_1 - \eta_3}$$

where

$\eta_x = \ln(k_x)$, $x = 1, 2, 3$, and $\eta_m = \frac{(\eta_1 + \eta_2 + \eta_3)}{3}$

The shape of the ellipsoid ranges from perfectly oblate ($T_j = +1$) to perfectly prolate ($T_j = -1$) (Jelinek 1981).

In this study, AMS data were collected from a total of 127 sample sites, both within the laccolith (119 sample sites) and three adjacent inclined sheets (08 sample sites) to determine magma flow patterns and investigate the relationship in emplacement dynamics between the laccolith and adjacent inclined sheets (e.g., Fig. 2a). Although the sampling localities across the laccolith were partly determined by outcrop accessibility, we ensured samples were collected across the length and height of the laccolith. An excellently exposed but inaccessible, ~5 m thick sheet extends upwards from the northwest side of the laccolith, but we were able to collect two samples from the laccolith directly beneath (Fig. 3). Along the south-east laccolith margin we sample two sheets, henceforth referred to as Sheet 1 and Sheet 2, which are both ~8m wide (Fig 4).

For each sample site, we collected oriented blocks, which we drilled into 22 mm by 25 mm right cylinder core sub-specimens using a rock coring drill press and a diamond-tipped, nonmagnetic saw blade. The sub-specimen data was averaged for each block (Jelínek, 1978) to produce mean values of the AMS ellipsoid. The three principal axis directions for each block sample are plotted stereographically within 95% confidence limits so the measured axes have a high degree of confidence statistically thus the interpreted direction of each principal axis is deemed statistically valid. All AMS measurements were carried out using an automated 3D rotator attached to a KLY-5a Kappabridge operating at a low alternating field of 400A/m at 1220 HZ at the University of St. Andrews M^{3}Ore Laboratory. The localities of the sheets sampled are marked in Localities A and B within Figure 1.

Rock magnetic experiments

The interpretation of AMS data is subject to several caveats. For instance, if the magnetic signature of a sample were dominated by single-domain magnetite, an “inverse” AMS fabric where K_1 is orthogonal to the crystallographic long is expected (Potter and Stephenson 1988; Rochette *et al.*1999). If left undetected, the presence of inverse fabrics may compromise interpretation of the AMS fabric and the arising magma flow model (e.g., Hrouda and Ježek 2017). To aid the interpretation of AMS data, thermomagnetic experiments were conducted on 15 representative samples from across the intrusion to inform on the composition, grain size and domain state of the mineral phase(s) that control the AMS fabric (e.g., Hrouda *et al.* 1997).

Thermomagnetic experiments require each sample to be powdered in a ceramic pestle and mortar, a 0.3 g powder subsample underwent a three-step heating/cooling regime as follows: 1) heating from -196°C to 0°C using a CS-L cryostat KLY5-a attachment; 2) heating 25°C to 700°C and cooling back to 40°C using CS4 furnace attachment; and 3) a second heating treatment from -196°C to 0°C using a CS-L cryostat KLY5-a attachment. An argon atmosphere was maintained to minimise sample oxidisation during step 2. Curie point and Verwey transitions were estimated from the heating-cooling curves using either the Hopkinson Peak (Hopkinson 1890) or inflection point methods (Tauxe 1998); these transitions can be used to interpret the magnetic mineralogy of each sample and determine what mineral phases control the AMS response (Dunlop and Özdemir 1997). Thermomagnetic experiments were conducted at the M^{3}Ore Laboratory at the University of St. Andrews using an AGICO KLY-5a Kappabridge operating at 400A/m at 1220 HZ.

Results

Intrusion geometry and host rock deformation

Glacially incised valleys reveal a ~370 m thick section of the Reyðarártindur Laccolith downwards from its exposed roof contact (Fig. 2). While large parts of the roof and wall contacts are excellently exposed, the floor of the intrusion is not visible, so the plutons true thickness is unknown. The geometry of the laccolith is broadly defined by a domed-shaped, intrusion-induced forced fold (Figs 2, 3, and 4); i.e. the gentle WNW regional tilt of the lava pile is locally deflected to strike parallel to, and thus dip gently (~05–30º) away from, the exposed intrusion boundary defining a ~1 km wide structural aureole (Figs. 2 and 4a). The roof contact is generally flat lying to gently dipping (~00–15º) towards the NNE (Fig. 2).

NE-SW to NNE-SSW trending, steeply inclined fault/fracture arrays occur pervasively across the host rock, and subordinate WNW-ESE fault/fracture sets also occur less frequently (Figs 3a, and 4a). The NE-SW (striking between ~040–070°) to NNE-SSW (striking between ~350–020°) fault/fracture populations locally define a sigmoidal fault/fracture geometry, particularly in the host rock near the southern contact (Figs. 3a and 4a). Throughout the structural aureole, steeply inclined silicic sheets, which range from tens to hundreds of meters in length and between <1–12 m in thickness, are occasionally traced along the strike of these fault/fracture populations (Figs 3 and 4). These sheets are locally observed to extend directly outward from the main body of the laccolith (Figs. 3b and 4b). A section of NNE-SSW fault bounded lavas adjacent to the NW laccolith contact diverge from the predominantly outward, up-doming forced fold geometry and instead, dip gently to moderately inwards towards the main intrusion body (Figs. 2 and 3a, b).

Petrography of the Reyðarártindur Laccolith

The Reyðarártindur Laccolith consists mainly of porphyritic, granitoids, granophyres and banded rhyolites (Fig. 2). The “net-veined complex” is the lowest exposed structural level exposed in the intrusion and consists of a distinct, composite mafic-intermediate-felsic complex referred previously as the 'net-veined' complex in surrounding sub-volcanic intrusions (Fig. 2). This complex consists of a variety of mingling and mixing features where angular clasts, pillows, and tabular masses of dolerite and basaltic rock are embedded within a granophyric host.

Granitoids with relatively coarse plagioclase phenocrysts (~2–8 mm) occur immediately above the 'net-veined' complex in the topographically low exposure in the ENE of the laccolith. Most of the laccolith is composed of granitoids with granophyric/graphic textures of intergrown quartz and feldspars (e.g. Fig. 2). Phenocrysts of euhedral to subhedral plagioclase as well as occasional tabular orthoclase crystals (2–4 mm, 5-30 vol%) occur within an equigranular (<0.5–1.0 mm) groundmass of plagioclase, K-feldspar and quartz with minor amphibole and biotite. Zircon and Fe-Ti oxides also occur as accessory phases.

The banded rhyolitic texture generally outcrops in the structurally higher sections of the laccolith and in the inclined sheets offset from the laccolith in the NW section of the structural aureole (Fig. 2). The rhyolite consists of a similar mineralogical assemblage to the to the granitoids as well as occasional miarolitic cavities often filled with secondary minerals, mainly quartz. The flow-banding in the rhyolite is defined by thin bands (~1–5 mm) of aligned quartz and feldspar crystals as well as small-scale variations in groundmass crystallinity. Flow banding in the inclined sheets parallel the margins and while mostly appears planar, occasional open to tight folding of bands is observed.

Rock magnetic experiments

Continuous susceptibility versus temperature dependency experiments show two abrupt features on the heating-cooling curves (Fig. 5): (i) an abrupt increase in susceptibility between -175°C to approximately -150°C before the susceptibility curve plateaus up to the ambient room temperature, which marks a Verwey Phase transition where the magnetite crystal lattice changes from a monoclinic to cubic structure (Verwey and Haayman 1941) (Fig. 5a); and (ii) an abrupt decrease in susceptibility between 575-580°C (Fig. 5a) corresponding with the Curie temperatures (Tc) for a very low Ti titanomagnetite (0.1% < Ti content < 1.0%) or near-stoichiometric magnetite (Ti < 0.1%) as the dominant magnetic minerals (Fig 5a; Akimoto 1962; Tauxe 1998; Lattard *et al.* 2006; Getzlaff 2008). Several samples display a peak in susceptibility at ~470–480°C with a subsequent secondary peak at 575-580°C during heating (Fig. 5a), consistent with a low titanium titanomagnetite phase where exsolution of Ti between 500–700°C resulted in the removal of the 470–480°C peak on the cooling curve and a more prominent ~580°C magnetite curie point (Akimoto 1962; Dunlop and Özdemir 1997). A <10% increase in bulk susceptibility occurs between 270°C and 340°C in a small number of samples during heating, this feature is always absent on the cooling curve and a 5–20% increase in bulk susceptibility is observed after cooling (Fig. 5a). We associate this increase in susceptibility to the growth of new magnetite during the experiment and thus attribute the 270°C and 340°C heating curve inflection to the breakdown of an iron sulphide minerals such as pyrite (Dunlop and Özdemir 1997).

Anisotropy of Magnetic Susceptibility (AMS) results

General susceptibility behaviour, degree of Anisotropy, and AMS ellipsoid shape

The average bulk susceptibility (K_m; Jelinek 1981) of the 127 samples measured is 9.24 x 10^{-3} SI, ranging from 7.92 x 10^{-5} SI to 4.12 x 10^{-2} SI (Table 1). The 'net-veined' complex in the lowermost exposed section of the intrusion generally has higher K_m values (191 – 412 x 10^{-3} SI) (Fig. 5b, Table 1). The corrected degree of anisotropy (P_j; Jelinek 1981) varies between 1.004 and 1.088, averaging at 1.018 with no overall distinguishing pattern across the laccolith. Shape factor (T_j; Jelinek 1981) values vary between -0.94 and 0.91 with a 0.09 average; 52 samples are predominately prolate (T_j<1) and 72 are dominantly oblate (T_j>1) (Table 1). Both P_j and T_j values show no defined pattern with respect to K_m (Fig. 5b, c). This shows that the shape and orientation of the AMS fabric is independent of bulk susceptibility and the relative abundance of magnetite in this set of samples.

AMS Fabrics of the laccolith

A stereographic projection of all AMS fabric data reveal that K_1 trends throughout the entire laccolith predominantly plot along an NNE–SSW axis and are mainly clustered into gently (~0–36º) and steeply (~55–90º) inclined populations (Fig. 6). The gently plunging, NE-SW trending K_1 axes typically occur (Fig. 6): (i) along the south-eastern basal exposure of the laccolith (Locality B); (ii) within a NW-SE trending linear zone located towards the centre of the laccolith exposure; and (iii) near the base of inclined sheets that extend up from the north-western margin of the main laccolith (Locality A). Interspersed with these NE-SW trending, gently plunging K_1 axes are steeply inclined magnetic lineations with variable plunge directions (Fig. 6). For example, in Locality A, a concentration of steep NW-SE trending K_1 axes aligned adjacent to the NW contact (Fig. 6).

The K_3 axes (i.e. pole to K_1-K_2 plane) are also clustered into two distinct gently and steeply inclined populations in both the WNW/ ESE and centre of the stereonet respectively, emphasizing the dominant NNE-SSW strike of the magnetic foliation patterns across the laccolith (Fig. 7). Gentle to moderate dips of magnetic foliations typically occur at lower elevations along the lower intrusion margin and at an outlier to the northwest of the laccolith (Fig. 7). Several examples of magnetic fabrics that show no apparent relationship to the dominant NNE–SSW fabrics are noted across the laccolith (Figs. 6 and 7). For instance, magnetic foliations immediately bordering the exposed south-southeast contact or close to the roof in the centre of the intrusion often strike sub-parallel/parallel to the orientation of the adjacent contact (Fig. 7).

Across the laccolith, the trends of both the K_1 lineation and K_1-K_2 plane deviate from the general NE-SW trend, particularly close to the margins of the intrusion. For example, the K_1 vectors in the structurally lower north-northwest exposures (including both the ‘net-veined’ complex and the northwest outlier) occasionally trend shallowly towards the NNW, parallel to the magnetic foliation (Figs. 6 and 7). In other parts of the northwest exposure, particularly the structurally higher sections, lineations are generally, very steeply inclined and sub-vertical in places with the equivalent foliations striking very steeply towards the NE–SW (Fig. 7). Within the middle to NW exposure of the laccolith, a concentration of lineations trend gently to moderately towards the SW, with foliations orientated NNE–SSW, corresponding with the dominant NNE–SSW magnetic fabric axis (Fig. 8). Towards the southeast exposure, lineations locally plunge gently towards the SSE, sub-parallel to the NNW-SSE strike of the corresponding foliation (Figs. 6 and 7). Overall, in plan-view the plunge axis and strike of the magnetic lineations and foliations, respectively, appear to diverge towards the SW (Figs 6 and 7).

AMS fabrics from steeply inclined sheets

In the NW margin (Locality A) the AMS fabrics from the two samples directly below the sub-vertical sheet show magnetic lineations that plunge moderately toward the NE, roughly parallel to the nearby inferred contact of the sheet sampled. The foliation adjacent to the inferred NW margin strikes 257º with a moderate dip to the NNW (42º) while, near the inferred SE margin, the foliation strikes NW–SE, sub-perpendicular to the strike of the sheet with a moderate dip the NE (30º) (Fig. 8). The T_j values indicate triaxial (-0.026) and near prolate (-0.460) shapes from the northwest and southeast margins respectively in from the northwest to southeast margin respectively while, the P_j value is constant across both sample sites (1.018 – 1.021) (Fig. 8). The resultant vector perpendicular to the bisecting line between the two magnetic foliation planes taken indicates a sub-vertical flow that appears to be dip-parallel or slightly dip-oblique attitude the overlying sheet (Fig. 8).

Along the SE margin of the intrusion (Locality B), the magnetic foliation strikes for the three samples across Sheet 1 range from 216–240º with dip values ranging from moderately to steeply inclined (34–86º) to the NW across the sheet from southeast to northwest (Fig. 9). These NW and SE sample values are oblique to the strike of the respective sheet margins (217/64º, NW contact; 228/67º, SE contact) at angles 36º (NW contact) and 54º (SE Contact) (Fig. 9). The magnetic foliation of Sheet 2 shows a strike range of 203–211° with a relatively constant dip (62–63º) throughout (Fig. 9). The observed attitude of magnetic foliations, like Sheet 1, are also oblique with respect to their corresponding margins contact ranging from 13–16º (Fig 9). Along the southeast margin of both sites, the lineation is sub-parallel to the dip direction of the foliation, the plunge of the remaining K_1 axes across both sheets are variable, ranging from 06–54º and largely subparallel to the strikes of the magnetic foliations (Fig. 9). The trend and plunge of the K_1 and K_2 axes on the magnetic foliation planes vary across both sheets with triaxial to oblate fabrics in Sheet 1(T_j; 0.131 – 0.522) and more oblate fabrics in Sheet 2 (T_j; 0.424 – 0.669) (Fig. 9). The degree of oblateness (i.e. T_j) increases towards the centre of each sheet (Fig. 9). Both the K_m and P_j values also increase in magnitude towards the centre in both sheets (Fig. 9).

Discussion

Magnetic signature

The AMS patterns observed in this study allow us to infer the emplacement mechanism of the Reyðarártindur Laccolith. Magnetic experimental data combined with petrographic observations facilitate the comparison of AMS fabrics with true petrographic fabrics. Susceptibly vs temperature dependency experiment results (Fig. 5a) coupled with the relatively high Km values (Table 1) indicate that multidomain to pseudo-single-domain magnetite are the dominant magnetic minerals in the rock. The magnetic susceptibility of magnetite is multiple orders of magnitude great than other minerals (e.g., biotite) which contribute to the AMS signal, these data show that magnetite is the overwhelmingly dominant contributor to the AMS tensor (e.g., Fig. 5a; Borradaile and Jackson 2010). Therefore, all AMS fabrics are inferred as 'normal' and representative of the rock fabric (Rochette *et al.*1999; Ferré 2002).

Laccolith construction

Previous AMS analysis of other laccoliths has shown that their internal architecture can be sub-divided into lobe-shaped structures, defined by magnetic fabrics indicating lobe-lobe contacts where the lobes open out and have bulbous terminations (e.g., Cruden *et al.* 1999; Stevenson *et al.* 2007a ; Magee *et al.* 2012b). Here, we propose a similar mechanism where the moderately to steeply dipping magnetic foliations that curve around ~NNE-SSW lineation axes, as well as contact-parallel magnetic foliations peripheral to exposed contacts are interpreted to represent portions of coalesced, laterally flowing ‘tongue-like’ magma lobes (Fig. 10). The preservation of the NE-SW trending zone of steeply, and oppositely dipping magnetic foliations may be interpreted to record a boundary between two magma pulses (Stevenson *et al.* 2007a). Furthermore, the extrapolated convex south-westward foliation orientations within the lobes ‘wrap’ around the K_1 lineations, which are inferred to splay towards the NW or SE, and may mimic a frontal lobate geometry (Fig. 10a) (e.g., Stevenson *et al.* 2007a). Interpreting these magnetic foliations as being oriented parallel to lobe contacts would suggest that the lobes close towards WSW, and thus propagated from the NE (Fig. 10a, b). The outcrop dependency of sampling limits our interpretation of the exact known geometry and number of lobes present, but we suggest lobe sizes vary from <500-~2000 m wide (Fig. 10). Some of the variations in fabric orientations within the broadly defined lobes could relate to possible smaller scale subdivisions into subsidiary flow units (e.g., magma fingers; Thomson and Hutton 2004). The persevered lobe boundaries as evidenced by the steeply dipping magnetic foliation zones were not overprinted during lobe coalescence, suggesting little mixing occurred between the lobes and an internal boundary was maintained (e.g., Magee *et al.* 2012b; Tomek *et al.* 2019). Such preservation of emplacement-related fabrics and a lack of mixing between the inferred lobes may occur because each magma pulse had a different rheology, perhaps reflecting incremental intrusion and the cooling of one pulse before the other was injected (e.g., Magee *et al.* 2013a, 2016; Hoyer and Watkeys 2017). Emplacement of the lobes was spatially accommodated uplift of the overlying host rock resulting in gentle doming (forced folding) and intrusion-induced faulted adjacent to the laccolith (Figs. 2, 4, 9, 10) (e.g., Wilson *et al.* 2016). The true lengths of the long axes lobes are difficult to characterize as they appear to close underneath the host rock to the WSW and propagate from underneath the roof in the ENE.

Evacuation of magma from the laccolith

Our combined magnetic fabric and structural observations show that the inclined sheets studied are located on the lateral terminations of the lobes along their propagating edge? (Figs 10 and 11a and 12) The magma transport direction is interpreted at Locality A by measuring the direction of imbricated magnetic foliation planes sampled from either side of the overlying sheet contacts (Figs 9 and 11b). These results suggest that magma was redirected from the laterally emplaced lobes within the main body of the laccolith to steeply inclined NE-SW trending sheet ascent in the overlying SE dipping sheet (Figs 9 and 11). Additionally, immediately to the south of this sheet within the rhyolithic zone adjacent to the NW Margin, relatively steep magnetic lineations occur in a linear NE-SW segment in several sections of the west-northwest margin of the laccolith (Figs 6 and 10 and 11). These lineations are mostly sub-parallel to parallel with the dip directions of the corresponding magnetic foliations, which all strike NE-SW direction parallel to the main flow axis of the magma lobes in the laccolith (Figs. 6, 7 and 10). In most cases, these fabrics appear to structurally and topographically overlie the preserved laterally flowing magma lobes, which in the northwest of the laccolith are inferred to be propagating towards the NNW (Fig. 10). These observations imply that the rhyolite zone outcropping parallel to the NW margin forms part of the inclined sheet along the propagating edge of the laccolith further underlying that magma ascent from the magma lobes occurred via peripheral sheets.

Magnetic foliations in the two sheets measured in the southeast of the laccolith (Locality B) are generally subparallel or slightly oblique to sheet contacts (i.e. NNW-SSE) (Figs 8 and 12a,b). Across both sheets, the slightly to moderately oblate magnetic fabrics (Tj: 0.131–0.669; see Fig. 8 and 12b) and the 95% confidence ellipses of the K_1 and K_2 axes overlap, thus making the K_1 lineation ill-defined and unsuitable as a proxy for the flow or stretching direction (e.g., Fig. 8; Cañón-Tapia 2004; Cañón-Tapia and Herrero-Bervera 2009). K_3 mean axes are well defined, broadly perpendicular to the sheet margins, and are thus considered "normal magnetic fabrics" (Rochette *et al.* 1999); i.e. the K_1-K_2 planes (the magnetic foliation perpendicular to K_3 axes) are interpreted as the inferred magmatic foliation in the sheets (e.g., Rochette *et al*. 1992). We propose that magma flowed moderately to steeply upward within these sheets, along the plane of the magnetic foliation (perpendicular to orientation of the K_3 axes) and thus slightly oblique to the attitude of the sheet margins (Figs 8 and 12b). As both the sheet contacts and the inferred flow direction dip towards the main body of the laccolith, it is therefore likely that the magma ascending via the sheets was derived from the lobes within the laccolith itself. The slight obliqueness of the magnetic foliation (Fig. 12b) with respect to the sheet margins could indicate a some syn-emplacement shear movement of the sheet wall (e.g., Correa-Gomes *et al.* (2001). In Sheet 1, the intersection between the relatively shallow dipping (34º) magnetic foliation plane in the SE contact with the centre and NW samples magnetic foliation planes can be interpreted to represent an imbrication fabric indicating steeply inclined downward flow plunging at ~76 º (Fig. 12b) (e.g., Aubourg *et al.* 2002; Delcamp *et al.* 2015). This flow regime could be due to a waning or cessation of magma supply from, or through cooling and magma contraction of, the laccolith causing it to deflate and draw back magma within the inclined sheets; i.e. downwards flow in some inclined sheets may have followed initial ascent (e.g., Knight and Walker 1988; (Aubourg *et al.* 2002).

Structural controls on magma evacuation from laccolith

Our magnetic fabric analysis suggests that magma likely evacuated the Reyðarártindur Laccolith primarily via inwardly inclined sheets, which emanate from the lateral terminations of the magma lobes (Figs 11 and 12). We note that the orientation and distribution of these inclined sheets mirrors that of the ~NNE-SSW trending, steeply inclined fault/fracture arrays pervasive across the study area. Because these faults/fractures are cross-cut by the laccolith, we suggest they formed prior to magma emplacement, although it is likely that some of the observed faults/fractures in the structural aureole formed in response to outer-arc extension during forced folding (e.g., Cosgrove and Hillier 2000; Wilson *et al.* 2016). The sigmoidal architecture of the two fault/fracture populations is consistent with a sinistral oblique rifting system, which we suggest may have developed during regional Neogene WNW-ESE extension (e.g., Fig.1; Torfason 1979; Martin and Sigmarsson 2010). Furthermore, magma transgression from the lobes up along the fault planes may have been promoted by uplift of the overlying host rock (e.g., forced folding) in the hanging wall due to intrusion inflation (Bédard *et al*. 2012; Magee *et al.* 2013b). This could produce a tensile σ_3 along the fault aiding its reactivation as a fault concordant magma conduit (e.g., Localities A and B; Figs 11, 12) (Magee *et al.* 2013b).

The lava piles that moderately dip inwards towards the main body of the laccolith (Locality A) may represent a tilted block morphology of the fault structure possibly suggest emplacement of the lobes occurred within the upper 500 m of the palaeosurface (e.g., Kettermann *et al.* 2019). Alternatively, this inward dip may be a product of sagging of the overlying roof structure as magma ascents upwards towards the ascent conduit. Overall, our observations compare with several studies demonstrating that pre-existing fault networks can provide preferential magma flow pathways in subvolcanic systems (Valentine and Krogh 2006; Thomson and Schofield 2008; Bédard *et al.* 2012; Magee *et al.* 2013b; Schofield *et al.* 2017; Mark *et al.* 2019; Morley 2018).

Implications

To improve volcanic hazard assessment, it is critical to understand how sub-volcanic plumbing systems are constructed and how their architecture controls eruption location and any intrusion-induced surface deformation patterns (e.g., Castro *et al.* 2016; Magee *et al.* 2017; Cruden and Weinberg 2018). Our work supports previous studies from igneous intrusions of variable compositions by showing: (i) laccolith (and sill) construction may be incremental, and that the entire intrusion may be compartmentalized into constituent lobes between which magma mixing is limited, potentially meaning the volume of magma monogenetic eruptions could tap may be restricted (e.g., Thomson and Hutton 2004; Schofield *et al.* 2012, 2017; Galland *et al.* 2019; Tomek *et al.* 2019); (ii) evacuation of magma along inclined sheets emanating from the lateral terminations of a laccolith may feed eruptions laterally offset from the main area of forced folding and surface deformation, which will be centred above the inflating laccolith (e.g., Thomson 2007; Jackson 2012; Galland *et al.* 2018; Schmiedel *et al.* 2019); and (iii) pre-existing faults can provide important ascent pathways for magma, potentially controlling eruption location (e.g., Valentine and Krogh, 2006; Gaffney *et al*. 2007; Bédard *et al.* 2012; Holford *et al*. 2012; Magee *et al.* 2013a, b); (Mark *et al.* 2019). Our study further emphasizes the importance to characterise the structural framework of active volcanic settings to monitor subsurface magma movement and location eruption.

Conclusions

Field, structural and rock magnetic observations reveal that the silicic Miocene, sub-volcanic Reyðarártindur Laccolith in SE Iceland comprises of incrementally emplaced, laterally extensive magma lobes that flowed, inflated and coalesced along a NE-SW primary axis. The layered lava piles in the surrounding structural aureole mostly exhibit an intrusion-induced domed-shaped, forced fold with steeply inclined, NNE-SSW left stepping en-echelon fault/fracture geometries pervasive across the aureole. The NNE-SSW fault/fracture population acted as preferential pathways for moderately to steeply inclined magma ascent directly from the magma lobes as observed by the geometric relationship between AMS fabrics and the margins of rhyolitic/granophyric sheets that regularly coincide with and intrude along the fault planes. Overall, our observations demonstrate the compartmentalization of a sub-volcanic laccolith into constituent, laterally propagating lobes where pre-existing faults can provide important ascent pathways for magma emanating from the lateral terminations of these lobes. Our observations have implications for monitoring volcanic hazard assessment as potential eruptions can be laterally offset from the laccolithic magma source and its overlying forced fold and surface deformation.

Acknowledgements

The authors would like to thank M. S. Petronis for his valuable discussions, comments and feedback. We would also like to thank A. Fernández Ferrer, J. Pomerantz, J. Grinham, R. Changleng and C. Gordon for their assistance and company in the field.

Funding

This study formed part of V. Twomeys's internally funded PhD research at the University of St. Andrews

Data availability statement

All data generated or analysed during this study are included in this published article and its Supplementary information files.

References

Akimoto, S. 1962. Magnetic properties of FeO-Fe2O3-TiO2 system as a basis of rock magnetism. *Journal of Physics Society Japan*, **17 Suppl.**, 706–710.

Alfaro, R., Brandsdóttir, B., Rowlands, D.P., White, R.S. and Gudmundsson, M.T. 2007. Structure of the Grímsvötn central volcano under the Vatnajökull icecap, Iceland. *Geophysical Journal International*, https://doi.org/10.1111/j.1365-246X.2006.03238.x.

Archanjo, C.J., Launeau, P. and Bouchez, J.L. 1995. Magnetic fabric vs. magnetite and biotite shape fabrics of the magnetite-bearing granite pluton of Gameleiras (Northeast Brazil). *Physics of the Earth and Planetary Interiors*, **89**, 63–75, https://doi.org/10.1016/0031-9201(94)02997-p.

Aubourg, C., Giordano, G., Mattei, M. and Speranza, F. 2002. Magma flow in sub-aqueous rhyolitic dikes inferred from magnetic fabric analysis (Ponza Island, W. Italy). *Physics and Chemistry of the Earth*, https://doi.org/10.1016/S1474-7065(02)00113-4.

Bédard, J.H., Naslund, H.R., et al. 2012. Fault-mediated melt ascent in a Neoproterozoic continental flood basalt province, the Franklin sills, Victoria Island, Canada. *Bulletin of the Geological Society of America*, https://doi.org/10.1130/B30450.1.

Bemis, S.P., Micklethwaite, S., Turner, D., James, M.R., Akciz, S., T. Thiele, S. and Bangash, H.A. 2014. Ground-based and UAV-Based photogrammetry: A multi-scale, high-resolution mapping tool for structural geology and paleoseismology. *Journal of Structural Geology*, https://doi.org/10.1016/j.jsg.2014.10.007.

Bodvarsson, G. and Walker, G.P.L. 1964. Crustal Drift in Iceland. *Geophysical Journal of the Royal Astronomical Society*, https://doi.org/10.1111/j.1365-246X.1964.tb06295.x.

Borradaile, G.J. and Jackson, M. 2010. Structural geology, petrofabrics and magnetic fabrics (AMS, AARM, AIRM). *Journal of Structural Geology*, **32**, 1519–1551, https://doi.org/10.1016/j.jsg.2009.09.006.

Burchardt, S., Tanner, D. and Krumbholz, M. 2012a. The Slaufrudalur pluton, southeast Iceland-An example of shallow magma emplacement by coupled cauldron subsidence and magmatic stoping. *Bulletin of the Geological Society of America*, https://doi.org/10.1130/B30430.1.

Burchardt, S., Tanner, D. and Krumbholz, M. 2012b. The Slaufrudalur pluton, southeast Iceland—An example of shallow magma emplacement by coupled cauldron subsidence and magmatic stoping. *Geological Society of America Bulletin*, **124**, 213–227, https://doi.org/10.1130/b30430.1.

Burchardt, S., Tanner, D.C., Troll, V.R., Krumbholz, M. and Gustafsson, L.E. 2012c. Three-dimensional geometry of concentric intrusive sheet swarms in the Geitafell and the

Dyrfjöll volcanoes, eastern Iceland. *Geochemistry, Geophysics, Geosystems*, https://doi.org/10.1029/2011GC003527.

Callot, J.P., Geoffroy, L., Aubourg, C., Pozzi, J.P. and Mege, D. 2001. Magma flow directions of shallow dykes from the East Greenland volcanic margin inferred from magnetic fabric studies. *Tectonophysics*, https://doi.org/10.1016/S0040-1951(01)00060-9.

Cañón-tapia, E. and Chávez-Álvarez, M.J. 2004. Theoretical aspects of particle movement in flowing magma: Implications for the anisotropy of magnetic susceptibility of dykes. *Geological Society Special Publication*, https://doi.org/10.1144/GSL.SP.2004.238.01.15.

Cañón-Tapia, E. 2004. Anisotropy of magnetic susceptibility of lava flows and dykes: A historical account. *Geological Society Special Publication*, https://doi.org/10.1144/GSL.SP.2004.238.01.14.

Cañón-Tapia, E. and Herrero-Bervera, E. 2009. Sampling strategies and the anisotropy of magnetic susceptibility of dykes. *Tectonophysics*, https://doi.org/10.1016/j.tecto.2008.11.012.

Castro, J.M., Cordonnier, B., Schipper, C.I., Tuffen, H., Baumann, T.S. and Feisel, Y. 2016. Rapid laccolith intrusion driven by explosive volcanic eruption. **7**, 13585.

Correa-Gomes, L.C., Souza Filho, C.R., Martins, C.J.F.N. and Oliveira, E.P. 2001. Development of symmetrical and asymmetrical fabrics in sheet-like igneous bodies: The role of magma flow and wall-rock displacements in theoretical and natural cases. *Journal of Structural Geology*, https://doi.org/10.1016/S0191-8141(01)00007-4.

Cosgrove, J.W. and Hillier, R.D. 2000. Forced-fold development within Tertiary sediments of the Alba Field, UKCS: Evidence of differential compaction and post-depositional sandstone remobilization. *Geological Society Special Publication*, https://doi.org/10.1144/GSL.SP.2000.169.01.05.

Cruden, A.R. and Weinberg, R.F. 2018. Mechanisms of magma transport and storage in the lower and middle crust-magma segregation, ascent and emplacement. *In*: *Volcanic and Igneous Plumbing Systems: Understanding Magma Transport, Storage, and Evolution in the Earth's Crust*, https://doi.org/10.1016/B978-0-12-809749-6.00002-9.

Cruden, A.R., Tobisch, O.T. and Launeau, P. 1999. Magnetic fabric evidence for conduit-fed emplacement of a tabular intrusion: Dinkey Creek Pluton, central Sierra Nevada batholith, California. *J. Geophys. Res.*, **104**, 10511–10530, https://doi.org/10.1029/1998jb900093.

de Saint-Blanquat, M., Habert, G., Horsman, E., Morgan, S.S., Tikoff, B., Launeau, P. and Gleizes, G. 2006. Mechanisms and duration of non-tectonically assisted magma emplacement in the upper crust: The Black Mesa pluton, Henry Mountains, Utah. *Tectonophysics*, https://doi.org/10.1016/j.tecto.2006.07.014.

Delcamp, A., Petronis, M.S. and Troll, V.R. 2015. Discerning magmatic flow patterns in shallow-level basaltic dykes from the NE rift zone of Tenerife, Spain, using the Anisotropy of Magnetic Susceptibility (AMS) technique. *Geological Society Special Publication*, https://doi.org/10.1144/SP396.2.

Dunlop, D.J. and Özdemir, Ö. 1997. *Rock Magnetism*.

Eriksson, P.I., Riishuus, M.S., Sigmundsson, F. and Elming, S.Å. 2011. Magma flow directions inferred from field evidence and magnetic fabric studies of the Streitishvarf composite dike in east Iceland. *Journal of Volcanology and Geothermal Research*, https://doi.org/10.1016/j.jvolgeores.2011.05.009.

Eriksson, P.I., Riishuus, M.S. and Elming, S.A. 2015. Magma flow and palaeo-stress deduced from magnetic fabric analysis of the Álftafjördur dyke swarm: Implications for shallow crustal magma transport in Icelandic volcanic systems. *Geological Society Special Publication*, https://doi.org/10.1144/SP396.6.

Féménias, O., Diot, H., Berza, T., Gauffriau, A. and Demaiffe, D. 2004. Asymmetrical to symmetrical magnetic fabric of dikes: Paleo-flow orientations and Paleo-stresses recorded on feeder-bodies from the Motru Dike Swarm (Romania). *Journal of Structural Geology*, https://doi.org/10.1016/j.jsg.2003.12.003.

Ferré, E.C. 2002. Theoretical models of intermediate and inverse AMS fabrics. *Geophysical Research Letters*, **29**, 1127, https://doi.org/10.1029/2001gl014367.

Furman, T., Meyer, P.S. and Frey, F. 1992. Evolution of Icelandic central volcanoes: evidence from the Austurhorn intrusion, southeastern Iceland. *Bulletin of Volcanology*, **55**, 45–62, https://doi.org/10.1007/BF00301119.

Gaffney, E.S., Damjanac, B. and Valentine, G.A. 2007. Localization of volcanic activity: 2. Effects of pre-existing structure. *Earth and Planetary Science Letters*, https://doi.org/10.1016/j.epsl.2007.09.002.

Galland, O., Bertelsen, H.S., et al. 2018. Storage and transport of magma in the layered crust-formation of sills and related flat-lying intrusions. *In*: *Volcanic and Igneous Plumbing Systems: Understanding Magma Transport, Storage, and Evolution in the Earth's Crust*, https://doi.org/10.1016/B978-0-12-809749-6.00005-4.

Galland, O., Spacapan, J.B., et al. 2019. Structure, emplacement mechanism and magma-flow significance of igneous fingers – Implications for sill emplacement in sedimentary basins. *Journal of Structural Geology*, https://doi.org/10.1016/j.jsg.2019.04.013.

Geoffroy, L., Callot, J.P., Aubourg, C. and Moreira, M. 2002. Magnetic and plagioclase linear fabric discrepancy in dykes: A new way to define the flow vector using magnetic foliation. *Terra Nova*, https://doi.org/10.1046/j.1365-3121.2002.00412.x.

Geoffroy, L., Aubourg, C., Callot, J.P. and Barrat, J.A. 2007. Mechanisms of crustal growth in large igneous provinces: The north Atlantic province as a case study. *Special Paper of the Geological Society of America*, https://doi.org/10.1130/2007.2430(34).

Getzlaff, M. 2008. *Fundamentals of Magnetism*, https://doi.org/10.1007/978-3-540-31152-2.

Gudmundsson, A. 2012. Magma chambers: Formation, local stresses, excess pressures, and compartments. *Journal of Volcanology and Geothermal Research*, **237**–**238**, 19–41, https://doi.org/10.1016/j.jvolgeores.2012.05.015.

Hjartardóttir, Á.R., Einarsson, P., Bramham, E. and Wright, T.J. 2012. The Krafla fissure swarm, Iceland, and its formation by rifting events. *Bulletin of Volcanology*, https://doi.org/10.1007/s00445-012-0659-0.

Holford, S., Schofield, N., MacDonald, J., Duddy, I. and Green, P. 2012. Seismic analysis of igneous systems in sedimentary basins and their impacts on hydrocarbon prospectivity: examples from the southern Australian margin. *The APPEA Journal*, https://doi.org/10.1071/aj11017.

Hopkinson, J. 1890. Magnetic Properties of Alloys of Nnickel and Iron. *Proceedings of the Royal Society of London*, **48**, 1–13.

Horsman, E., Broda, R.J., Gwyn, N.Z., Maurer, E.A., Thornton, E.D. and Ward, M.T. 2018. Progressive Construction of Laccolithic Intrusive Centers: Henry MountainsHenry Mountains, Utah, U.S.A. *In*: *Advances in Volcanology*, https://doi.org/10.1007/11157_2016_18.

Hoyer, L. and Watkeys, M.K. 2017. Using magma flow indicators to infer flow dynamics in sills. *Journal of Structural Geology*, https://doi.org/10.1016/j.jsg.2017.02.005.

Hrouda, F. and Ježek, J. 2017. Role of single-domain magnetic particles in creation of inverse magnetic fabrics in volcanic rocks: A mathematical model study. *Studia Geophysica et Geodaetica*, https://doi.org/10.1007/s11200-015-0675-6.

Hrouda, F., Jelínek, V. and Zapletal, K. 1997. Refined technique for susceptibility resolution into ferromagnetic and paramagnetic components based on susceptibility temperature-variation measurement. *Geophysical Journal International*, https://doi.org/10.1111/j.1365-246X.1997.tb04506.x.

Jackson, C.A.L. 2012. Seismic reflection imaging and controls on the preservation of ancient sill-fed magmatic vents. *Journal of the Geological Society*, https://doi.org/10.1144/0016-76492011-147.

Jelinek, V. 1981. Characterization of the magnetic fabric of rocks. *Tectonophysics*, **79**, T63----T67, https://doi.org/10.1016/0040-1951(81)90110-4.

Jelínek, V. 1978. Statistical processing of anisotropy of magnetic susceptibility measured on groups of specimens. *Studia geophysica et geodaetica*.

Johnson, A.M. and Pollard, D.D. 1973. Mechanics of growth of some laccolithic intrusions in the Henry mountains, Utah, I. Field observations, Gilbert’s model, physical properties and flow of the magma. *Tectonophysics*, https://doi.org/10.1016/0040-1951(73)90050-4.

Kettermann, M., Weismüller, C., von Hagke, C., Reicherter, K. and Urai, J.L. 2019. Large near-surface block rotations at normal faults of the Iceland rift: Evolution of tectonic caves and dilatancy. *Geology*, https://doi.org/10.1130/G46158.1.

Klausen, M.B. 2004. Geometry and mode of emplacement of the Thverartindur cone sheet swarm, SE Iceland. *Journal of Volcanology and Geothermal Research*, https://doi.org/10.1016/j.jvolgeores.2004.05.022.

Klausen, M.B. 2006. Geometry and mode of emplacement of dike swarms around the Birnudalstindur igneous centre, SE Iceland. *Journal of Volcanology and Geothermal Research*, https://doi.org/10.1016/j.jvolgeores.2005.09.006.

Knight, M.D. and Walker, G.P.L. 1988. Magma flow directions in dikes of the Koolau complex, Oahu, determined from magnetic fabric studies (Hawaii). *Journal of Geophysical Research*, https://doi.org/10.1029/JB093iB05p04301.

Koch, F.G., Johnson, A.M. and Pollard, D.D. 1981. Monoclinal bending of strata over laccolithic intrusions. *Tectonophysics*, **74**, T21----T31, https://doi.org/http://dx.doi.org/10.1016/0040-1951(81)90189-X.

Lattard, D., Engelmann, R., Kontny, A. and Sauerzapf, U. 2006. Curie temperatures of synthetic titanomagnetites in the Fe-Ti-O system: Effects of composition, crystal chemistry, and thermomagnetic methods. *Journal of Geophysical Research*, **111**.

Magee, C., Stevenson, C., O'Driscoll, B., Schofield, N. and McDermott, K. 2012a. An alternative emplacement model for the classic Ardnamurchan cone sheet swarm, NW Scotland, involving lateral magma supply via regional dykes. *Journal of Structural Geology*, https://doi.org/10.1016/j.jsg.2012.08.004.

Magee, C., Stevenson, C.T.E., Driscoll, B.O. and Petronis, M.S. 2012b. Local and regional controls on the lateral emplacement of the Ben Hiant Dolerite intrusion, Ardnamurchan (NW Scotland). *Journal of Structural Geology*, **39**, 66–82, https://doi.org/10.1016/j.jsg.2012.03.005.

Magee, C., O'driscoll, B., Petronis, M.S., Stevenson, C.T.E., Clay, P.L. and Gertisser, R. 2013a. Magma rheology variations in sheet intrusions of the Ardnamurchan Central Complex (Scotland) inferred from gabbro inclusion characteristics. *Journal of Petrology*, https://doi.org/10.1093/petrology/egs064.

Magee, C., Jackson, C.A.L. and Schofield, N. 2013b. The influence of normal fault geometry on igneous sill emplacement and morphology. *Geology*, https://doi.org/10.1130/G33824.1.

Magee, C., O'Driscoll, B., Petronis, M.S. and Stevenson, C.T.E. 2016. Three-dimensional magma flow dynamics within subvolcanic sheet intrusions. *Geosphere*, **12**, 842–866, https://doi.org/10.1130/GES01270.1.

Magee, C., Bastow, I.D., de Vries, B. van W., Jackson, C.A.L., Hetherington, R., Hagos, M. and Hoggett, M. 2017. Structure and dynamics of surface uplift induced by incremental sill emplacement. *Geology*, **45**, 431–434, https://doi.org/10.1130/G38839.1.

Mark, N.J., Holford, S.P., Schofield, N., Eide, C.H., Pugliese, S., Watson, D.A. and Muirhead, D. 2019. Structural and lithological controls on the architecture of igneous intrusions: Examples from the NW australian shelf. *Petroleum Geoscience*, https://doi.org/10.1144/petgeo2018-067.

Martin, E. and Sigmarsson, O. 2010. Thirteen million years of silicic magma production in Iceland: Links between petrogenesis and tectonic settings. *Lithos*, https://doi.org/10.1016/j.lithos.2010.01.005.

Mattson, S.R., Vogel, T.A. and Wilband, J.T. 1986. Petrochemistry of the silicic-mafic complexes at Vesturhorn and Austurhorn, Iceland: evidence for zoned/stratified magma. *Journal of Volcanology and Geothermal Research*, https://doi.org/10.1016/0377-0273(86)90023-5.

Mattsson, T., Burchardt, S., Almqvist, B.S.G. and Ronchin, E. 2018. Syn-emplacement fracturing in the sandfell laccolith, eastern iceland—implications for rhyolite intrusion growth and volcanic hazards. *Frontiers in Earth Science*, https://doi.org/10.3389/feart.2018.00005.

McCarthy, W., Petronis, M.S., Reavy, R.J. and Stevenson, C.T.E. 2015a. Distinguishing diapirs from inflated plutons; an integrated rock magnetic, magnetic fabric and structural study on the Roundstone Pluton, western Ireland. *Journal of the Geological Society, London*, https://doi.org/10.1144/0016-76492014-067.

McCarthy, W., Reavy, R.J., Stevenson, C.T. and Petronis, M.S. 2015b. Late Caledonian transpression and the structural controls on pluton construction; New insights from the Omey Pluton, western Ireland. *Earth and Environmental Science Transactions of the Royal Society of Edinburgh*, https://doi.org/10.1017/S1755691015000201.

Menand, T. 2008. The mechanics and dynamics of sills in layered elastic rocks and their implications for the growth of laccoliths and other igneous complexes. *Earth and Planetary Science Letters*, https://doi.org/10.1016/j.epsl.2007.11.043.

Michel, J., Baumgartner, L., Putlitz, B., Schaltegger, U. and Ovtcharova, M. 2008. Incremental growth of the Patagonian Torres del Paine laccolith over 90 k.y. *Geology*, https://doi.org/10.1130/G24546A.1.

Morgan, S., Stanik, A., Horsman, E., Tikoff, B., de Saint Blanquat, M. and Habert, G. 2008. Emplacement of multiple magma sheets and wall rock deformation: Trachyte Mesa intrusion, Henry Mountains, Utah. *Journal of Structural Geology*, https://doi.org/10.1016/j.jsg.2008.01.005.

Morley, C.K. 2018. 3-D seismic imaging of the plumbing system of the Kora Volcano, Taranaki Basin, New Zealand: The influence of syn-rift structure on shallow igneous intrusion architecture. *Geosphere*, https://doi.org/10.1130/GES01645.1.

Padilla, A.J., Miller, C.F., et al. 2016. Elucidating the magmatic history of the Austurhorn silicic intrusive complex (southeast Iceland) using zircon elemental and isotopic geochemistry and geochronology. *Contributions to Mineralogy and Petrology*, https://doi.org/10.1007/s00410-016-1279-z.

Pálmason, G. 2015. Model of crustal formation in Iceland, and application to submarine mid-ocean ridges. *In*: *The Western North Atlantic Region*, https://doi.org/10.1130/dnag-gna-m.87.

Petronis, M.S. and O'Driscoll, B. 2013. Emplacement of the early Miocene Pinto Peak intrusion, Southwest Utah, USA. *Geochemistry, Geophysics, Geosystems*, https://doi.org/10.1002/2013GC004930.

Petronis, M.S., Delcamp, A. and van Wyk de Vries, B. 2013. Magma emplacement into the Lemptégy scoria cone (Chaîne Des Puys, France) explored with structural, anisotropy of magnetic susceptibility, and Paleomagnetic data. *Bulletin of Volcanology*, https://doi.org/10.1007/s00445-013-0753-y.

Philpotts, A.R. and Philpotts, D.E. 2007. Upward and downward flow in a camptonite dike as recorded by deformed vesicles and the anisotropy of magnetic susceptibility (AMS). *Journal of Volcanology and Geothermal Research*, https://doi.org/10.1016/j.jvolgeores.2006.11.006.

Pollard, D.D., Muller, O.H. and Dockstader, D.R. 1975. The form and growth of fingered sheet intrusions. *Bulletin of the Geological Society of America*, https://doi.org/10.1130/0016-7606(1975)86<351:TFAGOF>2.0.CO;2.

Porreca, M., Cifelli, F., Soriano, C., Giordano, G. and Mattei, M. 2015. Magma flow within dykes in submarine hyaloclastite environments: An AMS study of the Miocene Cabo de Gata volcanic units. *Geological Society Special Publication*, https://doi.org/10.1144/SP396.14.

Potter, D.K. and Stephenson, A. 1988. Single domain particles in rocks and magnetic fabric analysis. *Geophysical Research Letters*, **15**, 1097–1100, https://doi.org/10.1029/GL015i010p01097.

Robertson, J.H. 1985. Physical properties of crystals: their representation by tensors and matrices by J. F. Nye . *Acta Crystallographica Section A Foundations of Crystallography*, https://doi.org/10.1107/s0108767385001477.

Rocchi, S., Westerman, D.S., Dini, A., Innocenti, F. and Tonarini, S. 2002. Two-stage growth of laccoliths at Elba Island, Italy. *Geology*, https://doi.org/10.1130/0091-7613(2002)030<0983:TSGOLA>2.0.CO;2.

Rochette, P., Jackson, M. and Aubourg, C. 1992. Rock magnetism and the interpretation of anisotropy of magnetic susceptibility. *Reviews of Geophysics*, https://doi.org/10.1029/92RG00733.

Rochette, P., Aubourg, C. and Perrin, M. 1999. Is this magnetic fabric normal? A review and case studies in volcanic formations. *Tectonophysics*, **307**, 219–234, https://doi.org/10.1016/s0040-1951(99)00127-4.

Roni, E., Westerman, D.S., Dini, A., Stevenson, C. and Rocchi, S. 2014. Feeding and growth of a dyke-laccolith system (Elba Island, Italy) from AMS and mineral fabric data. *Journal of the Geological Society*, https://doi.org/10.1144/jgs2013-019.

Saemundsson, K. 1980. Iceland. *Geology of the European countries: Denmark, Finland, Iceland, Norway, Sweden, (Bordas-Dunod, Paris; 26th International Geological Congress)*.

Schilling, J.G. 1973. Iceland mantle plume: Geochemical study of Reykjanes Ridge. *Nature*, https://doi.org/10.1038/242565a0.

Schmiedel, T., Galland, O., Haug, T., Dumazer, G. and Breitkreuz, C. 2019. Coulomb failure of Earth's brittle crust controls growth, emplacement and shapes of igneous sills, saucer-shaped sills and laccoliths. *Earth and Planetary Science Letters*, https://doi.org/10.1016/j.epsl.2019.01.011.

Schofield, N., Holford, S., et al. 2017. Regional magma plumbing and emplacement mechanisms of the Faroe-Shetland Sill Complex: implications for magma transport and petroleum systems within sedimentary basins. *Basin Research*, https://doi.org/10.1111/bre.12164.

Schofield, N.J., Brown, D.J., Magee, C. and Stevenson, C.T. 2012. Sill morphology and comparison of brittle and non-brittle emplacement mechanisms. *Journal of the Geological Society*, https://doi.org/10.1144/0016-76492011-078.

Sigmundsson, F., Parks, M., et al. 2018. Magma movements in volcanic plumbing systems and their associated ground deformation and seismic patterns. *In*: *Volcanic and Igneous Plumbing Systems: Understanding Magma Transport, Storage, and Evolution in the Earth's Crust*, https://doi.org/10.1016/B978-0-12-809749-6.00011-X.

Sparks, R.S.J., Biggs, J. and Neuberg, J.W. 2012. Monitoring volcanoes. *Science*, https://doi.org/10.1126/science.1219485.

Stevenson, C.T.E., Owens, W.H. and Hutton, D.H.W. 2007a. Flow lobes in granite: The determination of magma flow direction in the Trawenagh Bay Granite, northwestern Ireland, using anisotropy of magnetic susceptibility. *Geological Society of America Bulletin*, **119**, 1368–1386, https://doi.org/10.1130/b25970.1.

Stevenson, C.T.E., Owens, W.H., Hutton, D.H.W., Hood, D.N. and Meighan, I.G. 2007b. Laccolithic, as opposed to cauldron subsidence, emplacement of the Eastern Mourne pluton, N. Ireland: Evidence from anisotropy of magnetic susceptibility. *Journal of the Geological Society*, https://doi.org/10.1144/0016076492006-008.

Sturkell, E., Einarsson, P., Sigmundsson, F., Hreinsdóttir, S. and Geirsson, H. 2003. Deformation of Grímsvötn volcano, Iceland: 1998 eruption and subsequent inflation. *Geophysical Research Letters*, https://doi.org/10.1029/2002GL016460.

Sturkell, E., Einarsson, P., et al. 2006. Volcano geodesy and magma dynamics in Iceland. *Journal of Volcanology and Geothermal Research*, https://doi.org/10.1016/j.jvolgeores.2005.07.010.

Tarling, D.H. and Hrouda, F. 1993. The Magnetic Anisotropy of Rocks Tarling, D. and Hrouda, F. (eds). *Chapman & Hall, New York*, **54**, 2429–2442.

Tauxe, L. 1998. Paleomagnetic principles and practice. *Kluwer Academic Publishers, Dordrecht*, 299.

Thomson, K. 2007. Determining magma flow in sills, dykes and laccoliths and their implications for sill emplacement mechanisms. *Bulletin of Volcanology*, https://doi.org/10.1007/s00445-007-0131-8.

Thomson, K. and Hutton, D. 2004. Geometry and growth of sill complexes: Insights using 3D seismic from the North Rockall Trough. *Bulletin of Volcanology*, https://doi.org/10.1007/s00445-003-0320-z.

Thomson, K. and Schofield, N. 2008. Lithological and structural controls on the emplacement and morphology of sills in sedimentary basins. *Geological Society Special Publication*, https://doi.org/10.1144/SP302.3.

Thorarinsson, S.B. and Tegner, C. 2009. Magma chamber processes in central volcanic systems of Iceland: Constraints from layered gabbro of the Austurhorn intrusive complex. *Contributions to Mineralogy and Petrology*, https://doi.org/10.1007/s00410-009-0379-4.

Tomek, F., Gilmer, A.K., Petronis, M.S., Lipman, P.W. and Foucher, M.S. 2019. Protracted Multipulse Emplacement of a Postresurgent Pluton: The Case of Platoro Caldera Complex (Southern Rocky Mountain Volcanic Field, Colorado). *Geochemistry, Geophysics, Geosystems*, https://doi.org/10.1029/2019GC008477.

Torfason, H. 1979. Investigations into the structure of south-eastern Iceland. **I**, 589.

Valentine, G.A. and Krogh, K.E.C. 2006. Emplacement of shallow dikes and sills beneath a small basaltic volcanic center - The role of pre-existing structure (Paiute Ridge, southern Nevada, USA). *Earth and Planetary Science Letters*, https://doi.org/10.1016/j.epsl.2006.04.031.

Verwey, E.J.W. and Haayman, P.W. 1941. Electronic conductivity and transition point of magnetite (‘Fe3O4’). *Physica*, https://doi.org/10.1016/S0031-8914(41)80005-6.

Vollgger, S.A. and Cruden, A.R. 2016. Mapping folds and fractures in basement and cover rocks using UAV photogrammetry, Cape Liptrap and Cape Paterson, Victoria, Australia. *Journal of Structural Geology*, **85**, 168–187, https://doi.org/http://dx.doi.org/10.1016/j.jsg.2016.02.012.

Walker, G.P.L. 1974. The Structure of Eastern Iceland. *In*: *Geodynamics of Iceland and the North Atlantic Area*, https://doi.org/10.1007/978-94-010-2271-2_12.

Weismüller, C., Urai, J.L., Kettermann, M., Von Hagke, C. and Reicherter, K. 2019. Structure of massively dilatant faults in Iceland: Lessons learned from high-resolution unmanned aerial vehicle data. *Solid Earth*, https://doi.org/10.5194/se-10-1757-2019.

Wilson, P.I.R., McCaffrey, K.J.W., Wilson, R.W., Jarvis, I. and Holdsworth, R.E. 2016. Deformation structures associated with the Trachyte Mesa intrusion, Henry Mountains, Utah: Implications for sill and laccolith emplacement mechanisms. *Journal of Structural Geology*, https://doi.org/10.1016/j.jsg.2016.04.001.

Figure Captions

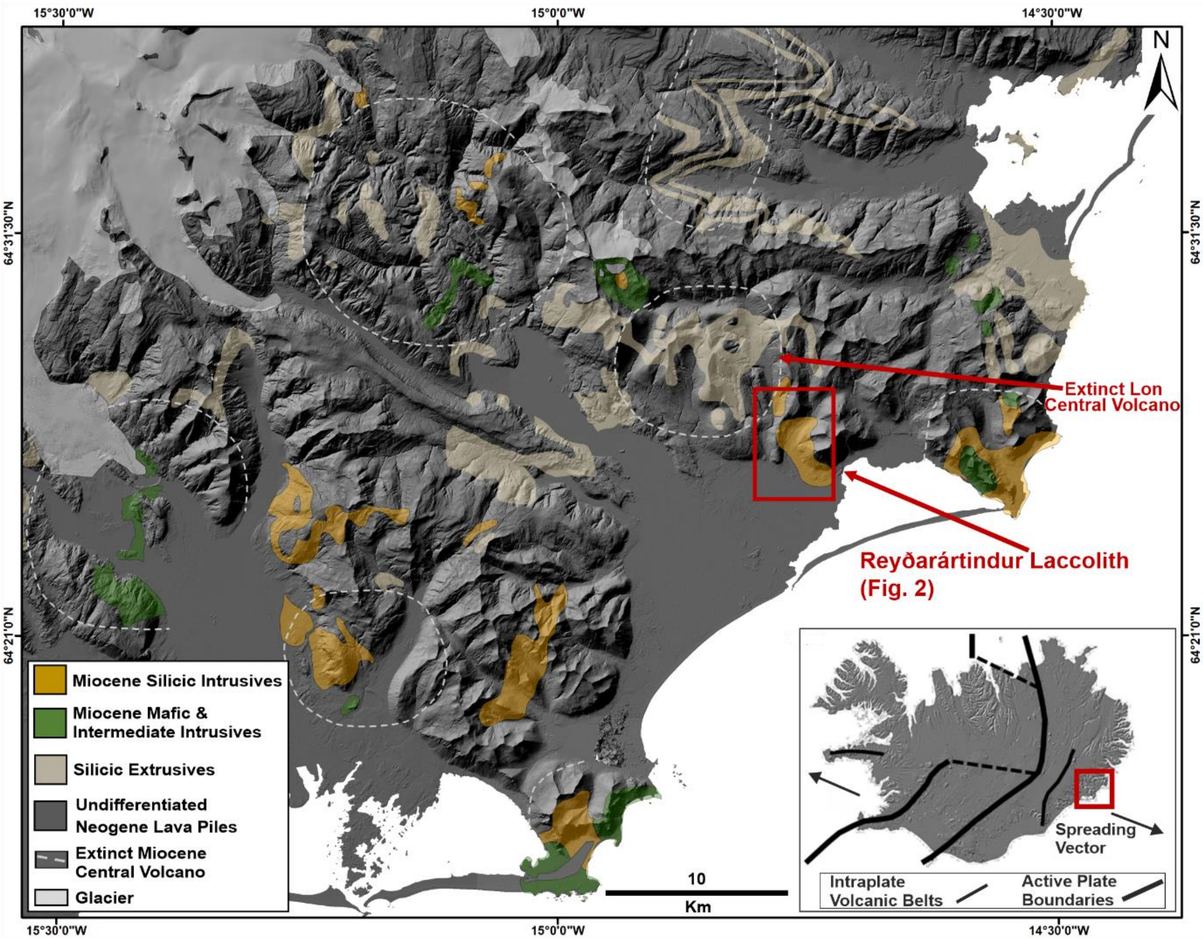

Fig.1. Simplified geological map of exposed Miocene volcanic systems in SE Iceland highlighting sub-volcanic magma bodies and extinct central volcano localities. (After Walker, 1974). Basemap based on data from the National Land Survey of Iceland, http://atlas.lmi.is/mapview/?application=DEM.

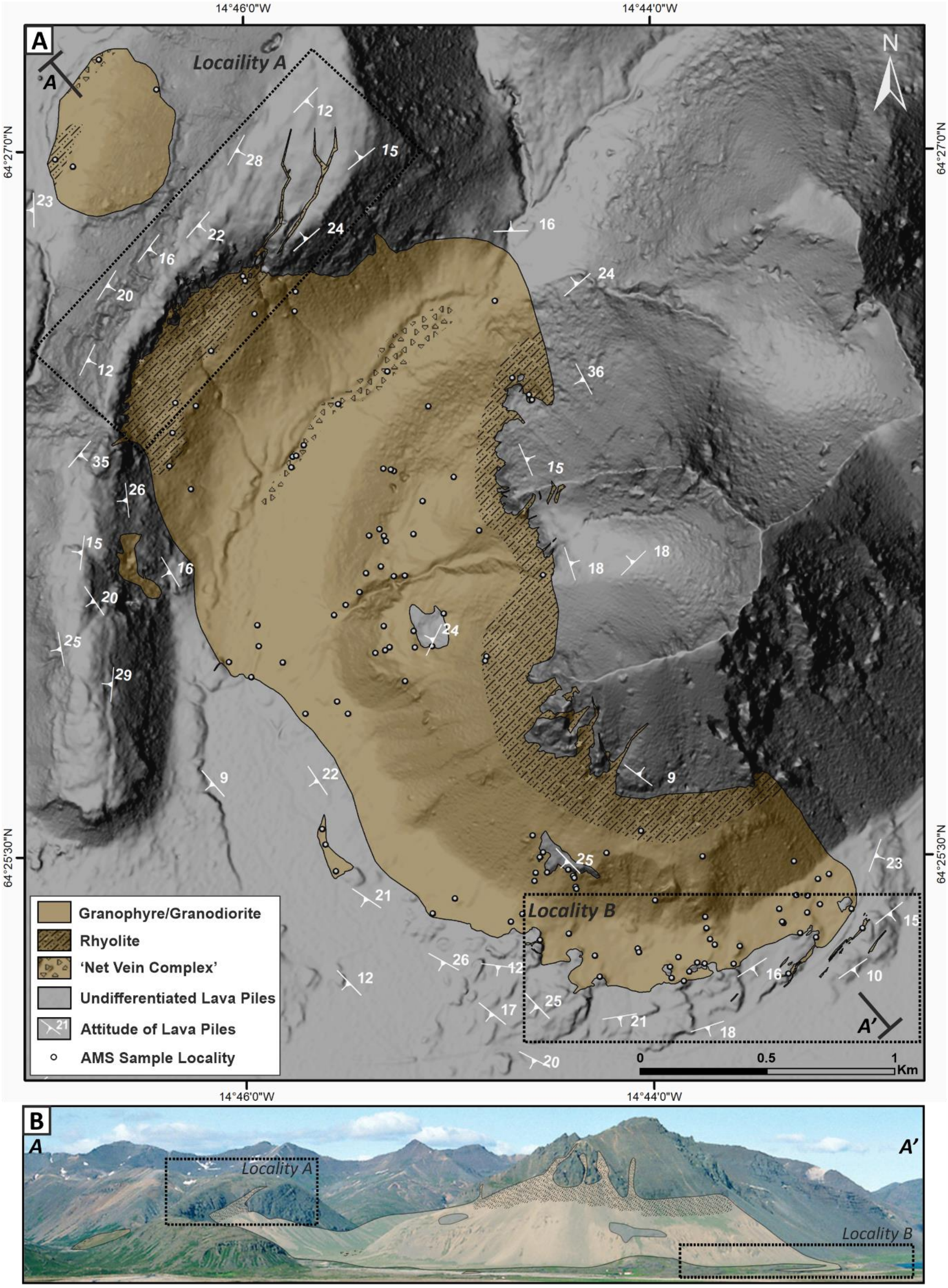

Fig.2. (A) Geological map of the Reyðarártindur Laccolith showing facies distribution, general geometry and surrounding attitude of layered lava piles which define a gently domed forced fold. (B) Photograph looking towards NE showing showing simple schematic of 3D cross-sectional exposure of the laccolith. Localities A and B referred to in text highted in dashed boxes.

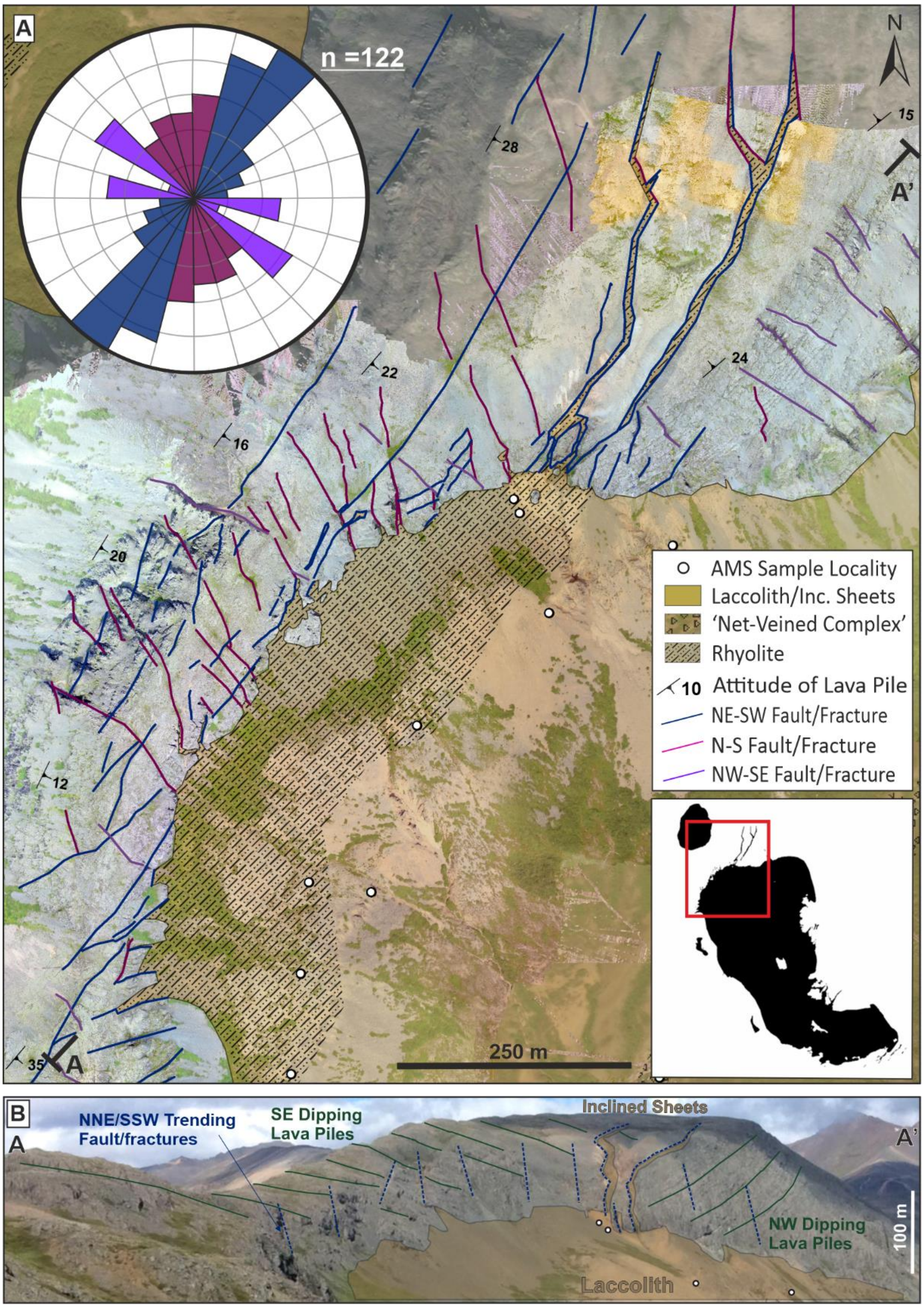

Fig.3. (A) High resolution orthophotograph of the north western exposure (Locality A) showing exposed contact of the Reyðarártindur Laccolith. Fault/Fracture sets mapped digitally within the exposed lava piles. Fractures and faults were classified into three sets and colour-coded based on their orientation and plotted on a rose plot (bin size 5^{o}). See supplementary data for full fault/fracture dataset. (B) Photograph looking towards the WNW showing gentle dip of lava piles above the laccolith and lava piles that dip inward towards the main body of the laccolith.

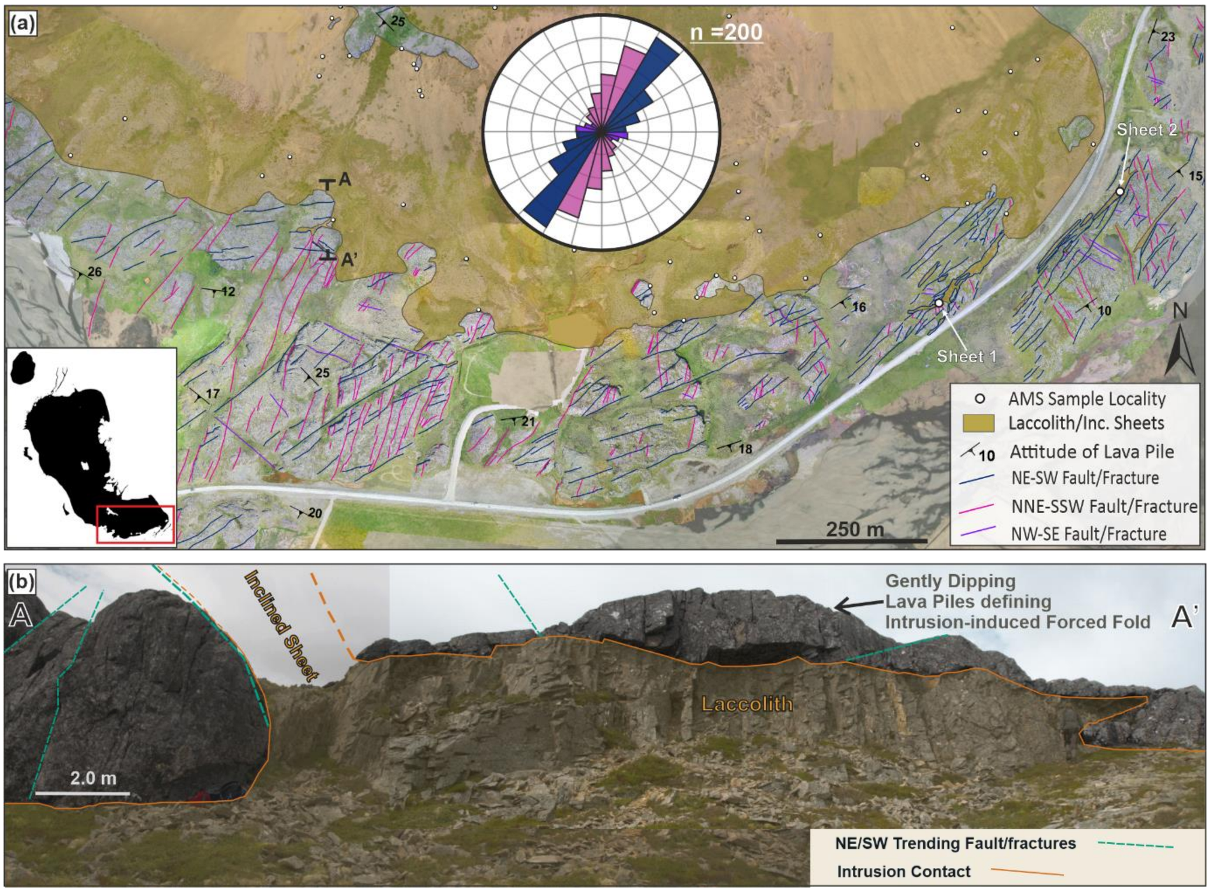

Fig.4. (A) High resolution orthophotograph of southern exposure (Locality B) showing exposed contact of the Reyðarártindur Laccolith. Fault/Fracture sets mapped digitally within the exposed lava piles. Fractures and faults were classified into three sets and colour-coded based on their orientation and plotted on a rose plot (bin size 5º). See supplementary data for full fault/fracture dataset. (B) Photograph looking towards the west showing gentle dip of lava piles above the main body of the laccolith as well as a NE-SW fault mediated steeply inclined sheet off shooting from the laccolith.

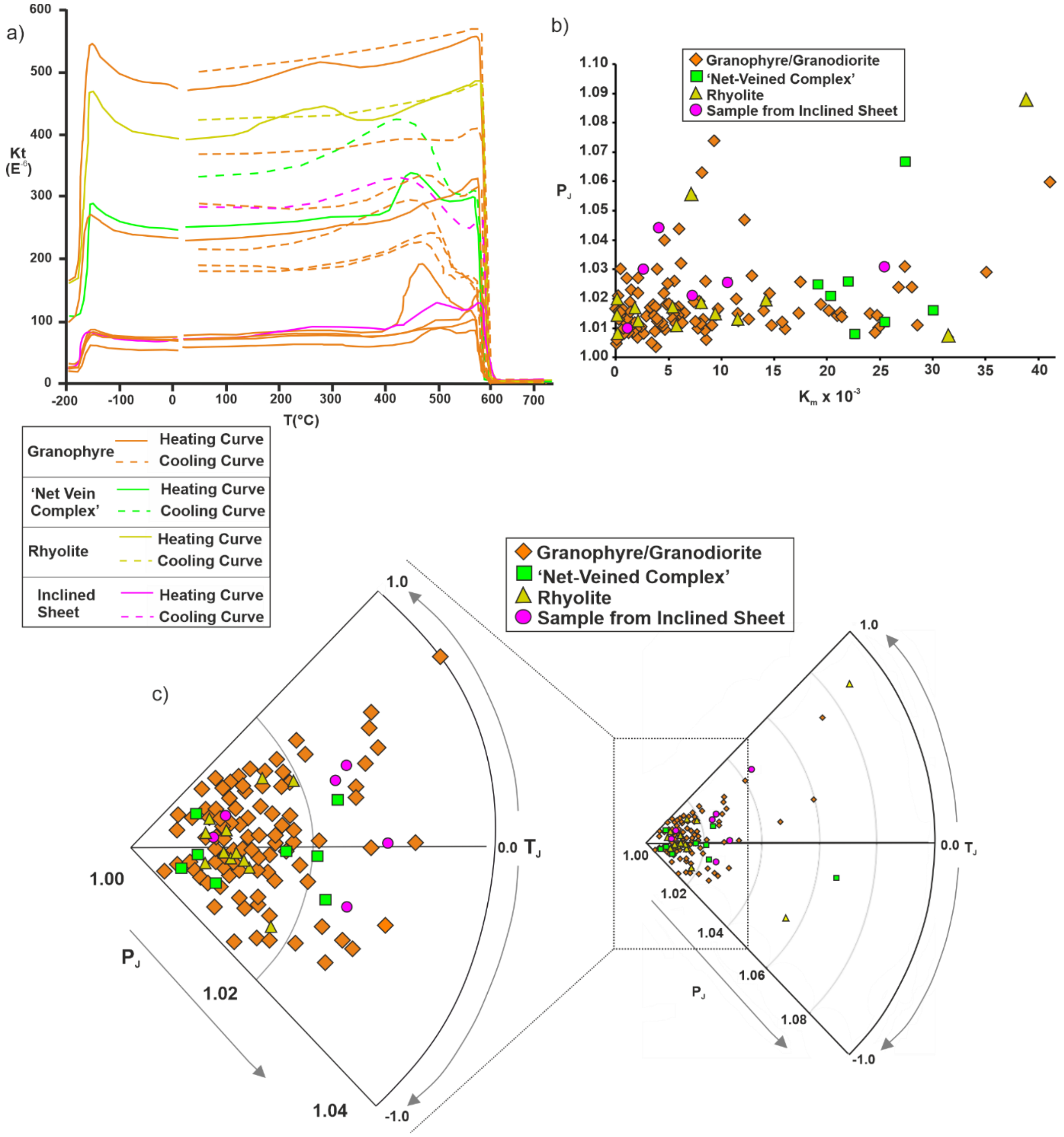

Fig.5. (a) Results of temperature dependant low-field magnetic susceptibility experiments from 6 representative AMS localities distributed across the intrusion. (b) P_j vs K_m plot with respect to the AMS tensor of each of the main facies across the laccolith. (c) Polar plot of T_j vs P_j data shows the spectrum of AMS tensor shape detected across the laccolith.

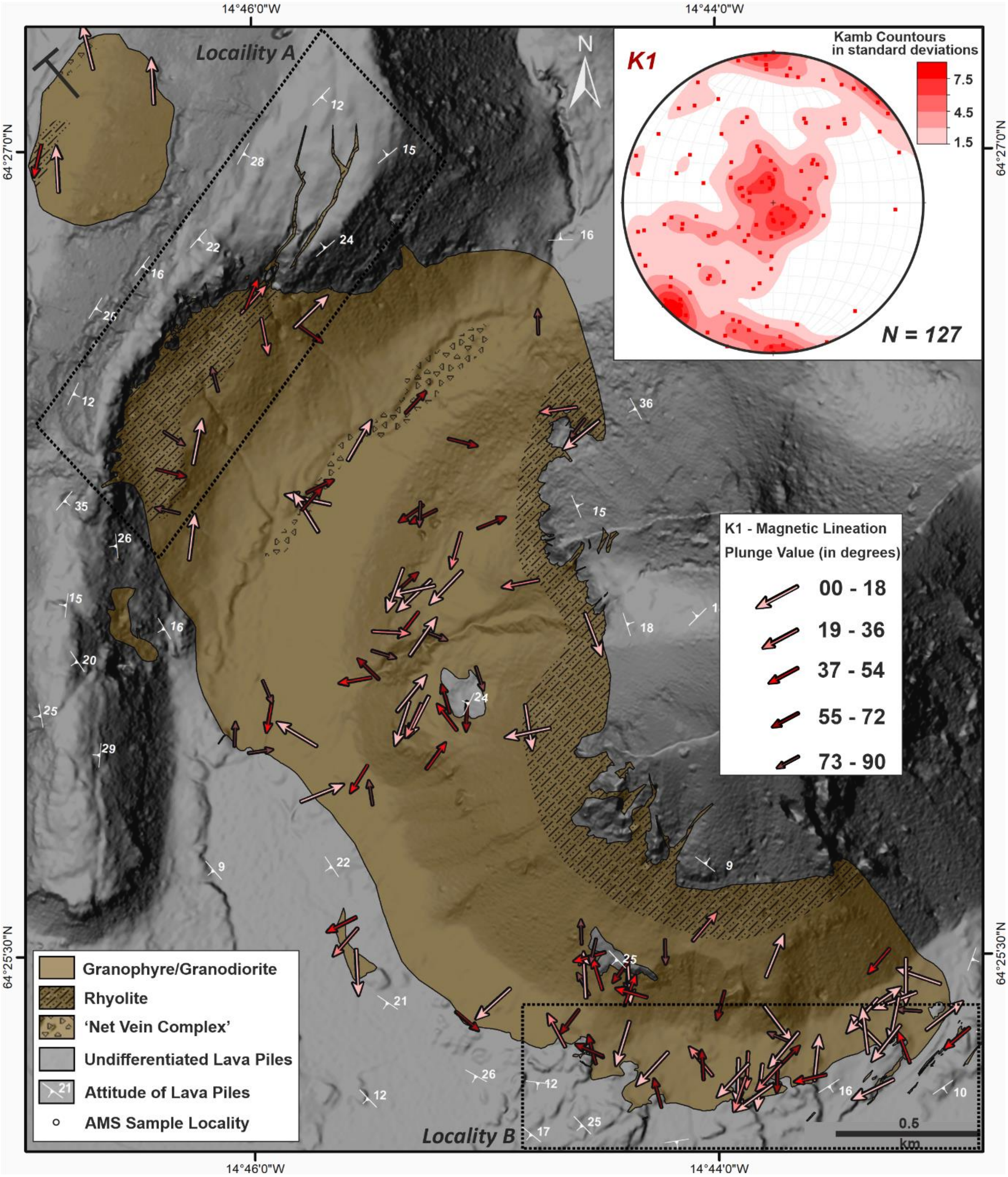

Fig.6. Map of Reyðarártindur Laccolith with results of K1 magnetic lineations from 127 sample localities. The degree of inclination of the K1 plunge is colour coded). Inset: Lower hemisphere, equal-area stereographic projection of K1 lineations showing the dominant NE-SW trend ranging from sub-horizontal to steeply inclined plunges.

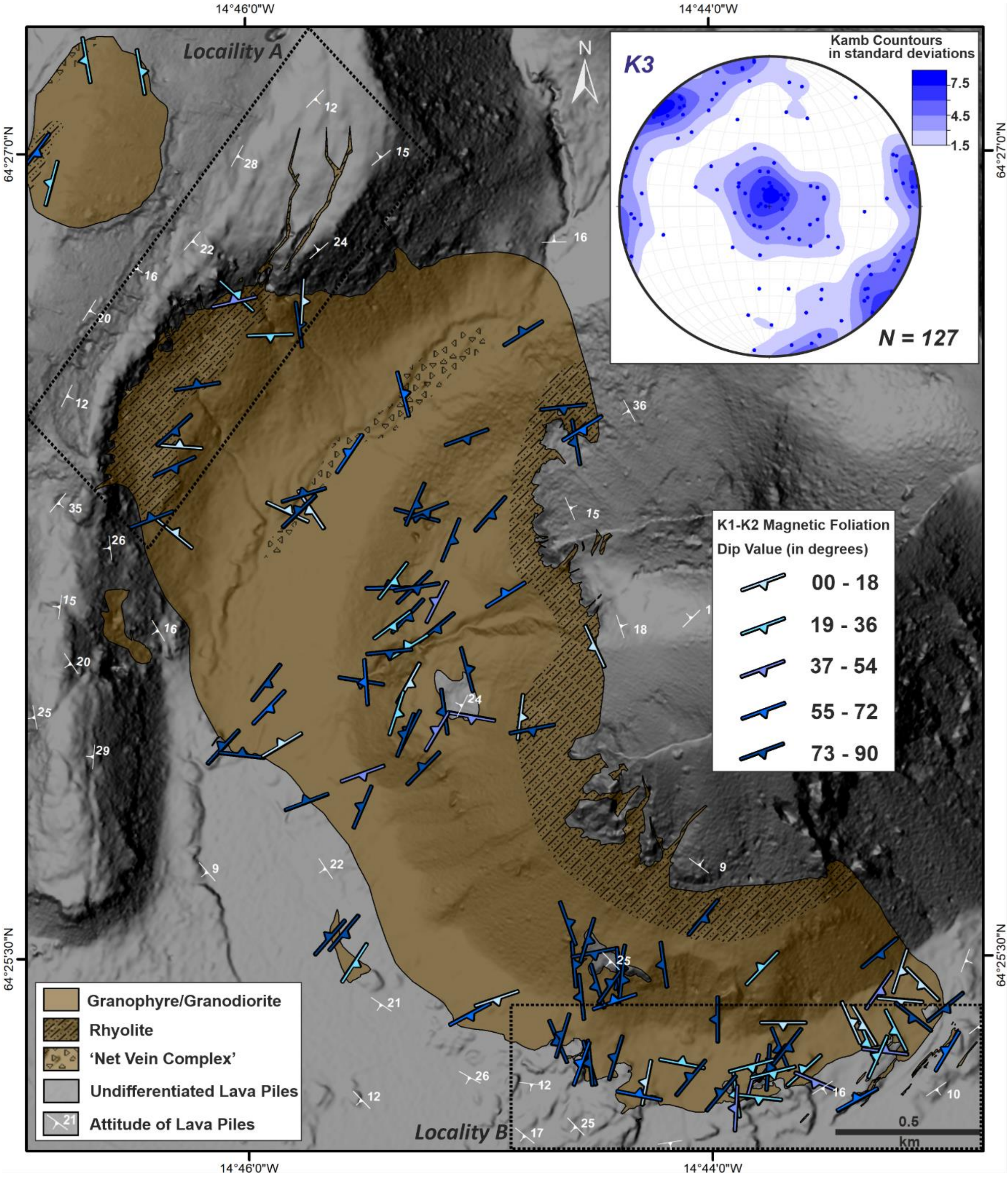

Fig.7. Map of Reyðarártindur Laccolith with results of K1-K2 (Magnetic Foliation) planes from 127 sample localities (The degree of dip of the magnetic foliation is colour coded). Inset: Lower hemisphere, equal-area stereographic projection of K3 AMS axis (pole to magnetic foliation plane) showing the dominant NE-SW trend of magnetic foliations ranging from sub-horizontal to steeply inclined plunges.

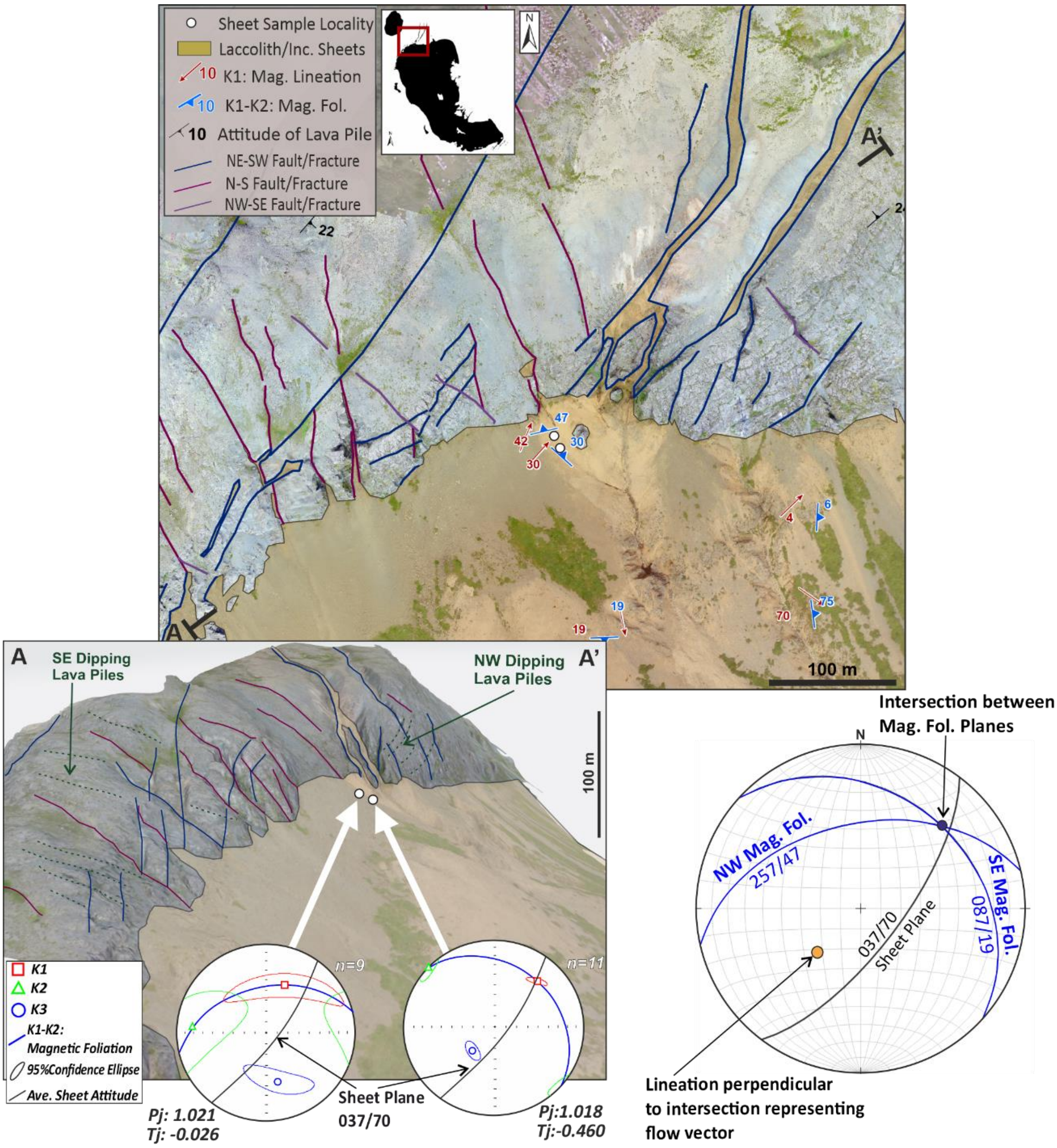

Fig.8. High resolution orthophotograph and field photograph of north western exposure of the Reyðarártindur Laccolith demonstrating relationship between NNE-SSW fault/fracture set and inclined sheets highlighting the localities of the AMS samples selected for imbrication directly beneath inclined sheet. Equal-area stereographic projections and Pj and Tj values from the AMS sample sites are also presented. A lower hemisphere equal area projection merging the two samples reveals and imbrication of the two magnetic foliation planes that indicates the direction and sense of inferred magma flow.

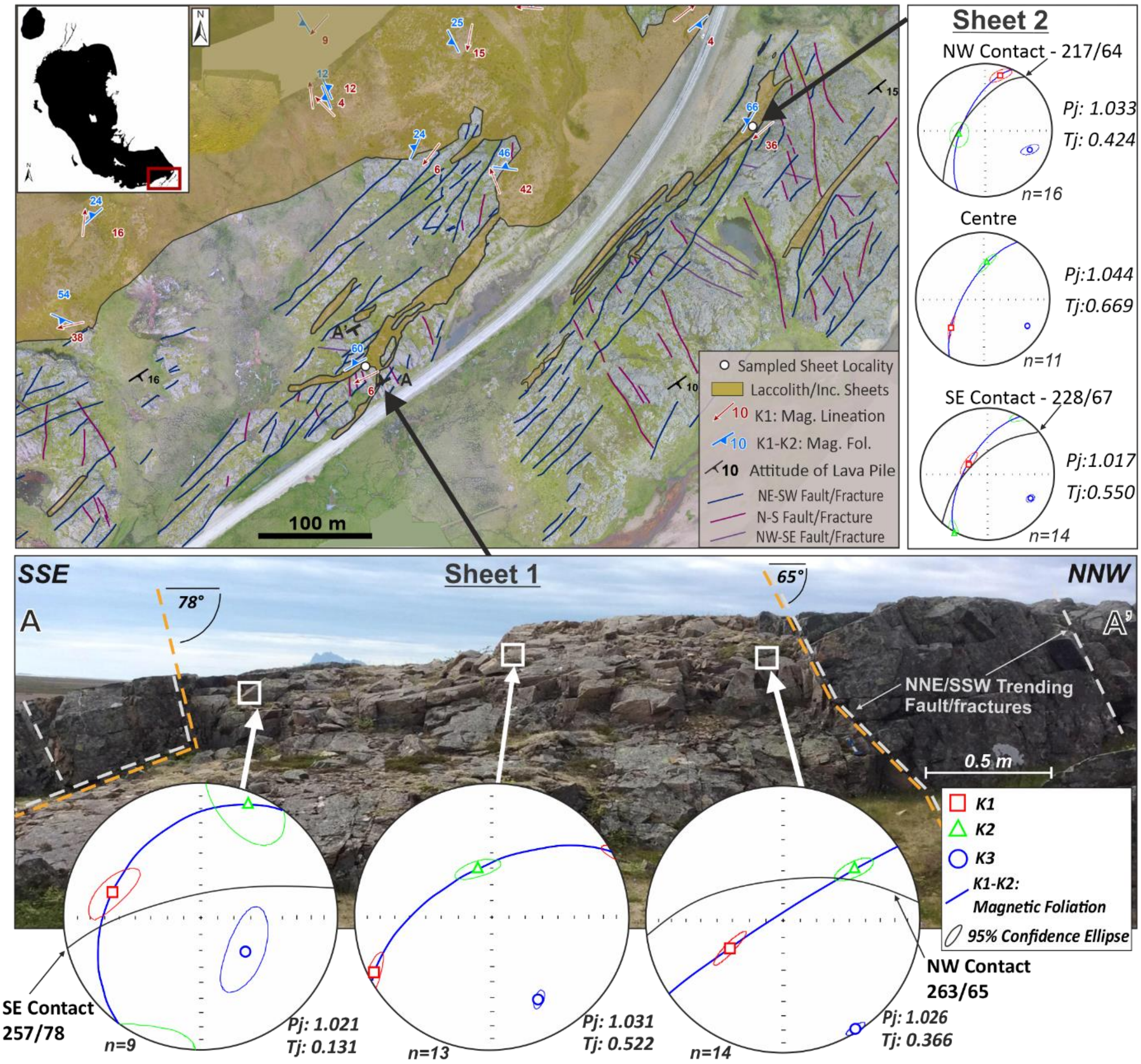

Fig.9. High resolution orthophotograph of the south exposure of the Reyðarártindur Laccolith demonstrating relationship between NNE-SSW fault/fracture set and inclined sheets and the localities of two of the sampled sheet sites. Equal-area stereographic projections and Pj and Tj values from the AMS sample sites that define the sample transect in each sheet. A field photograph of Sheet 1 looking towards the WSW shows the approximate distribution of the samples across the sheet.

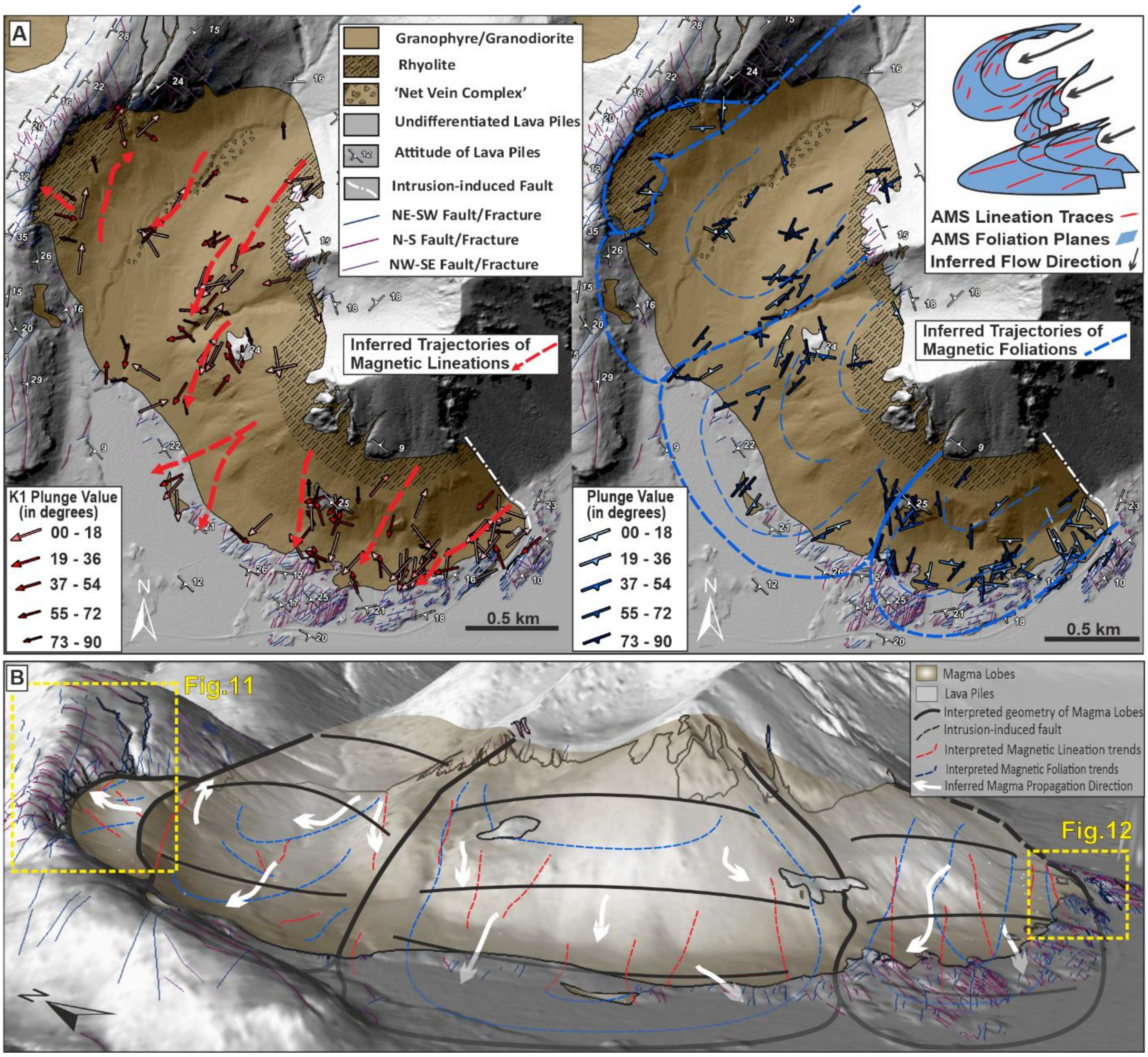

Fig,.10. (A) Maps showing orientation and distribution of AMS data in the Reyðarártindur Laccolith with dashed lines representing the inferred trajectories of magnetic lineations and foliations. Inset: 3D sketch showing the interpretation of magma lobes based on AMS data (Adapted from Stevenson et al., 2007a) (B) Division of the Reyðarártindur Laccolith into magmatic lobes that laterally propagated along a NE-SW axis.

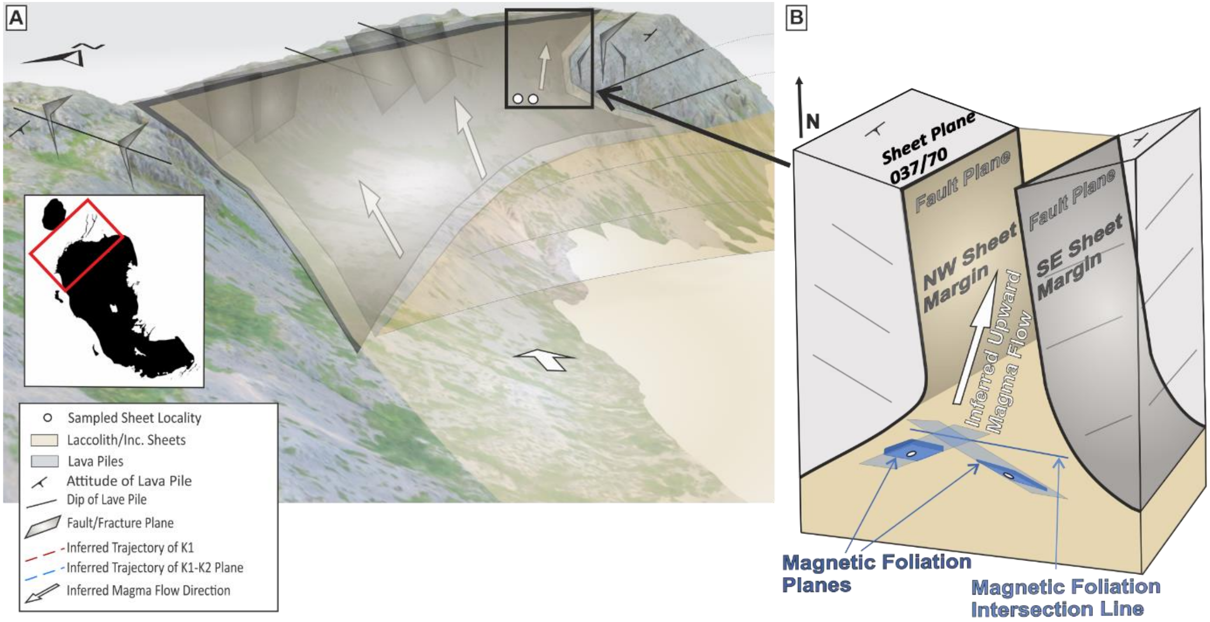

Fig. 11. (A) 3D projection of NW contact (Locality A) demonstrating NNE-striking fault controlled upward evacuation of magma on the periphery of NNE-SSW laterally propagating magma lobe. (B) Schematic depiction of the magnetic fabric imbrication relative to the overlying vent is also presented (e.g. Aubourg et al. 2002; Geoffroy et al. 2002).

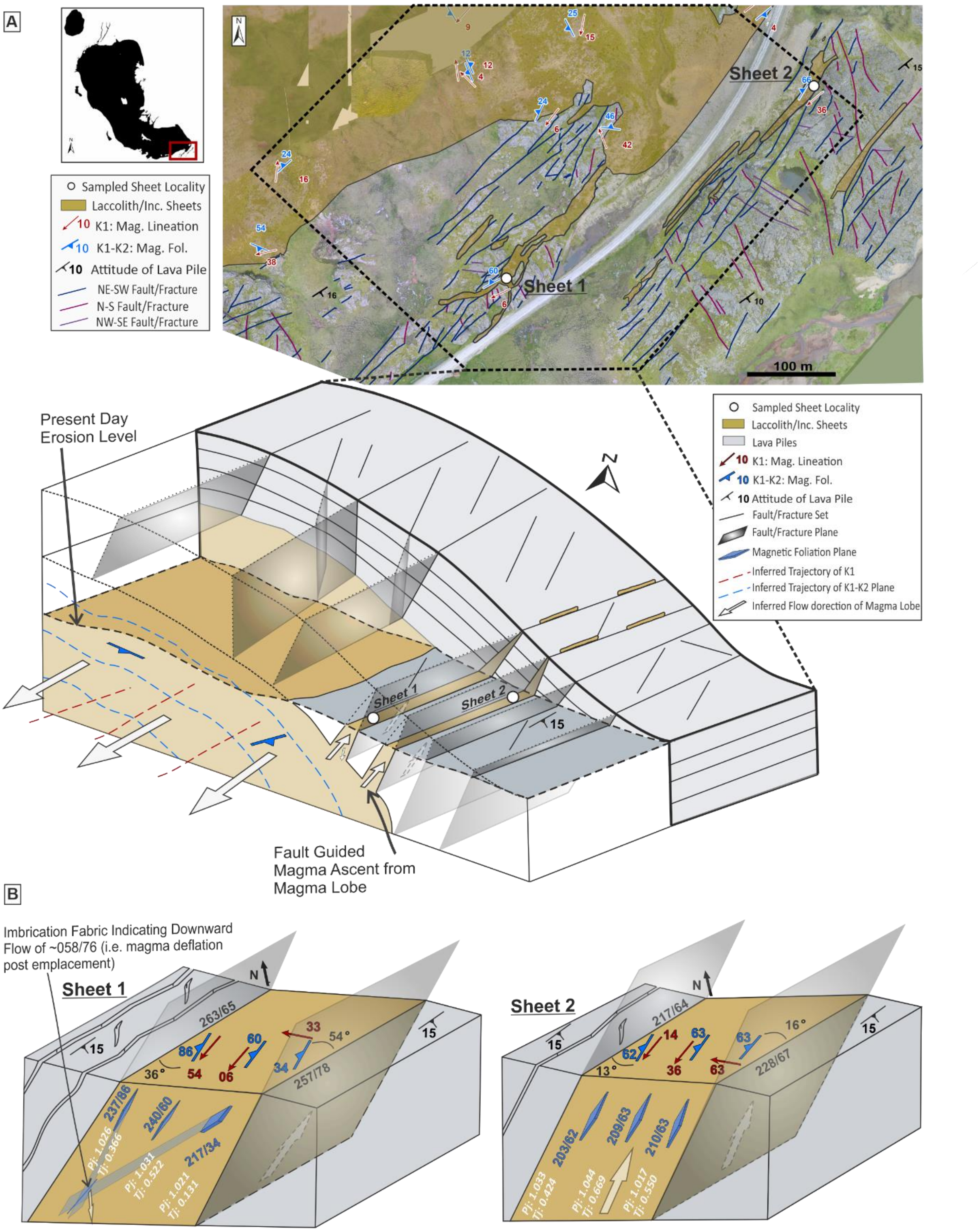

Fig. 12. (A) Block Diagram summarizing the fault mediated upward redirection of laterally propagating magma in the magma lobe from the SE Contact (Locality B). (B) Block diagrams showing AMS transects within sampled inclined sheets (Sheets 1 and 2).

Table Captions

Table 1. Anisotropy of Magnetic Susceptibility data from the Reyðarártindur Laccolith in SE Iceland

Site ID	Facies	East	North	n	K_1 Plunge	K_1 Trend	K_3 Plunge	K_3 Trend	Km x 10^{-03}	Pj	Tj
VT17RD002	Gr	512158.5	7145684	8	27	259	35	148	2.047	1.007	-0.343
VT17RD003	Gr	512058.2	7145895	7	69	068	10	312	3.753	1.009	0.437
VT17RD005	Gr	511935.1	7145800	4	19	196	17	292	2.860	1.014	0.089
VT17RD006	Gr	511899.6	7145670	6	12	224	54	117	4.111	1.012	0.876
VT17RD007	Gr	511790.3	7145642	6	00	227	17	317	7.834	1.01	-0.194
VT17RD008	Gr	511783.0	7145663	7	09	258	16	351	12.60	1.013	0.271
VT17RD009	Gr	511764.8	7145690	5	58	049	22	179	0.221	1.014	0.093
VT17RD010	Gr	511723.6	7145663	5	07	200	69	308	0.200	1.006	0.877
VT17RD011	Nv	511423.0	7145975	5	09	282	78	056	22.60	1.008	0.152
VT17RD012	Nv	511417.1	7145933	9	06	328	78	205	25.37	1.012	0.709
VT17RD013	Gr	512782.8	7144034	5	18	321	63	191	14.65	1.011	-0.004
VT17RD015	Gr	513358.5	7144135	7	12	315	62	068	7.926	1.019	0.441
VT18RD001	Gr	511171.2	7145164	17	72	002	12	133	2.162	1.022	0.579
VT18RD002	Ry	510949.8	7146069	11	62	104	18	335	5.665	1.016	-0.219
VT18RD003	Ry	510937.4	7145938	14	73	283	09	159	5.956	1.011	0.269
VT18RD004	Gr	511022.0	7145847	22	11	007	77	219	24.09	1.015	-0.168
VT18RD005	Gr	511259.3	7145105	14	73	082	04	186	4.804	1.018	0.106
VT18RD006	Gr	511289.3	7145227	9	45	190	29	314	1.098	1.027	0.007
VT18RD007	Nv	511466.7	7146021	13	58	064	05	163	22.02	1.026	-0.446
VT18RD008	Nv	511602.6	7146182	8	10	030	20	124	29.99	1.016	0.098
VT18RD009	Nv	511797.0	7146312	6	58	043	28	255	19.13	1.025	-0.605
VT18RD010	Ry	512288.9	7146286	9	32	262	03	354	14.33	1.019	-0.089
VT18RD011	Ry	512354.7	7146220	9	75	218	11	080	2.109	1.009	-0.191
VT18RD012	Ry	512366.9	7146199	12	13	231	25	328	0.285	1.021	-0.035
VT18RD013	Gr	511781.1	7145928	10	67	235	18	015	0.685	1.01	0.33
VT18RD014	Gr	511821.3	7145918	10	54	243	04	339	0.518	1.013	0.006
VT18RD015	Gr	511810.3	7145925	6	81	182	04	294	0.787	1.014	-0.549
VT18RD016	Gr	511958.5	7146174	14	69	104	13	340	3.363	1.005	-0.368
VT18RD017	Gr	512219.5	7146590	22	78	358	11	148	4.548	1.01	-0.042
VT18RD018	Gr	511384.1	7145164	9	12	301	76	149	41.17	1.06	0.263
VT18RD019	Gr	511473.6	7144961	14	11	068	08	159	17.53	1.026	0.396
VT18RD020	Gr	511640.3	7144961	8	76	351	08	113	6.274	1.032	0.018
VT18RD021	Gr	511041.9	7146175	14	16	011	73	184	14.46	1.022	0.665
VT18RD022	Ry	510960.6	7146188	9	77	123	12	318	11.62	1.015	-0.062
VT18RD023	Ry	511101.4	7146392	23	82	345	07	171	7.177	1.055	-0.558
VT18RD024	Ry	511235.2	7146669	11	30	042	60	222	1.753	1.017	-0.459
VT18RD025	Ry	511227.4	7146687	9	42	022	43	167	0.008	1.014	-0.056
VT18RD026	Gr	511273.4	7146539	20	19	169	71	358	21.21	1.015	-0.178
VT18RD027	Gr	511430.9	7146549	15	70	125	15	262	8.211	1.013	-0.467
VT18RD028	Gr	511434.5	7146627	12	04	046	84	273	5.953	1.012	0.019
VT18RD029	Gr	511974.5	7144173	10	70	130	20	332	8.532	1.006	-0.257
VT18RD030	Gr	512062.7	7144232	13	04	228	80	341	35.05	1.029	0.019
VT18RD031	Gr	512284.0	7144140	11	23	332	12	067	24.80	1.01	0.136
VT18RD032	Gr	511586.5	7145350	10	47	260	17	009	7.941	1.011	-0.109
VT18RD033	Gr	511771.2	7145542	11	49	218	03	313	5.532	1.012	0.414
VT18RD034	Gr	511865.5	7145506	8	82	112	08	321	5.532	1.014	-0.166
VT18RD035	Gr	511821.3	7145503	16	08	035	70	148	28.62	1.011	-0.235
VT18RD036	Gr	511711.5	7145515	13	20	093	61	323	5.970	1.017	-0.017
VT18RD037	Gr	511686.3	7145440	17	85	107	02	354	20.18	1.016	0.261
VT18RD038	Gr	511631.9	7145390	9	58	314	23	086	2.578	1.008	-0.406
VT18RD039	Ry	512411.1	7145508	16	01	159	81	065	31.49	1.007	0.572
VT18RD040	Gr	511900.4	7145288	9	58	344	05	082	12.91	1.028	0.366
VT18RD041	Gr	511905.2	7145223	7	42	323	46	121	13.95	1.016	0.275
VT18RD042	Gr	511805.0	7145223	15	04	207	08	117	5.884	1.015	-0.444
VT18RD043	Gr	511866.8	7145090	14	38	036	12	135	9.493	1.014	0.674
VT18RD044	Gr	511787.6	7145211	15	21	205	12	111	3.565	1.018	-0.677
VT18RD045	Gr	511593.9	7144339	9	12	177	70	303	0.445	1.03	-0.311
VT18RD046	Gr	511552.3	7144444	11	34	221	00	310	0.191	1.016	0.495
VT18RD047	Gr	511539.8	7144505	15	50	243	17	131	0.114	1.017	0.597
VT18RD048	Gr	511284.2	7145310	17	78	157	11	308	20.98	1.014	0.115
VT18RD049	Nv	511437.0	7145978	11	67	041	02	136	20.33	1.021	-0.59
VT18RD050	Gr	511599.2	7145009	11	38	212	38	340	4.440	1.011	-0.751
VT18RD052	Gr	511972.3	7145227	10	54	182	36	010	3.893	1.03	0.416
VT18RD053	Ry	512187.8	7145187	7	01	171	88	277	9.643	1.016	0.692
VT18RD054	Ry	512182.7	7145169	7	13	258	06	349	7.388	1.019	0.505
VT18RD055	Gr	512018.2	7145356	20	73	162	01	255	12.17	1.047	0.154
VT18RD056	Gr	511782.4	7145306	16	03	039	75	299	33.07	1.017	-0.726
VT18RD057	Gr	511749.0	7145201	14	00	198	60	288	24.81	1.014	-0.011
VT18RD058A	Gr	512396.0	7144072	13	70	293	19	110	2.132	1.027	-0.453
VT18RD058B	Gr	512398.8	7144068	12	71	296	14	074	5.865	1.014	0.101

VT18RD058C	Gr	512406.0	7144074	14	60	345	05	083	1.905	1.01	-0.011
VT18RD059	Gr	512328.6	7144170	10	68	218	08	107	8.537	1.026	0.228
VT18RD060	Gr	512376.3	7144301	14	77	331	05	084	1.237	1.015	-0.013
VT18RD061	Gr	512381.5	7144333	9	12	357	11	265	0.470	1.014	0.558
VT18RD062	Gr	512425.6	7144334	10	40	343	01	073	4.651	1.04	0.629
VT18RD063	Gr	512397.1	7144395	13	37	254	07	349	9.332	1.074	0.737
VT18RD064	Gr	512369.6	7144481	11	80	358	03	250	6.502	1.015	-0.403
VT18RD065	Gr	512410.9	7144414	5	84	193	01	287	0.287	1.015	-0.94
VT18RD066	Gr	512529.3	7144321	9	72	184	03	282	0.264	1.008	-0.283
VT18RD067	Gr	512533.9	7144313	7	06	176	09	267	0.032	1.016	0.054
VT18RD068	Gr	512509.6	7144346	9	64	217	01	125	3.809	1.017	0.133
VT18RD069A	Gr -Sh	513382.1	7143935	9	33	287	56	127	7.299	1.021	0.05
VT18RD069B	Gr -Sh	513378.4	7143935	13	06	244	30	151	25.48	1.031	0.58
VT18RD069C	Gr -Sh	513379.7	7143936	14	53	242	04	147	10.63	1.026	0.407
VT18RD070	Gr	513627.1	7144191	9	04	052	06	321	0.878	1.012	0.262
VT18RD071	Ry	512796.6	7144498	9	28	040	01	310	0.135	1.005	0.453
VT18RD072	Gr	513038.8	7144398	10	13	022	59	134	1.626	1.009	0.538
VT18RD075	Gr	512538.3	7144278	12	40	020	16	276	1.219	1.01	0.486
VT18RD076	Gr	512542.4	7144269	13	50	286	26	161	0.352	1.008	-0.239
VT18RD077	Gr	513537.3	7144328	8	04	289	81	045	1.258	1.01	0.905
VT18RD078	Gr	513493.2	7144308	13	01	180	85	288	1.365	1.019	0.632
VT18RD079	Gr	513453	7144243	12	05	249	79	005	1.236	1.009	0.141
VT18RD080	Gr	513502.5	7144209	10	77	274	08	038	0.274	1.013	0.105
VT18RD081	Gr	513451.9	7144177	10	15	191	65	063	1.020	1.013	0.72
VT18RD082	Gr	513409.2	7144245	16	16	056	51	305	15.83	1.012	0.23
VT18RD083	Gr	513341.9	7144191	7	09	222	81	059	5.551	1.026	0.279
VT18RD084	Gr	513352.5	7144140	11	04	353	78	246	26.78	1.024	0.25
VT18RD085	Gr	513185.7	7144044	12	16	006	66	138	21.43	1.014	-0.53
VT18RD086	Gr	513050.2	7144160	9	11	143	77	000	1.889	1.012	0.79
VT18RD087	Gr	513054.2	7144115	10	76	293	10	068	1.476	1.023	-0.416
VT18RD088	Gr	513068.7	7144071	9	04	220	27	128	2.469	1.01	0.286
VT18RD089	Gr	513087.8	7144050	8	60	044	03	308	7.618	1.012	0.527
VT18RD090	Gr	513047.8	7143975	14	61	182	02	274	17.40	1.015	0.336
VT18RD091	Gr	512512.1	7144093	12	12	197	01	107	9.132	1.011	0.283
VT18RD094	Gr	512614.2	7144006	18	04	223	83	101	28.10	1.024	0.351
VT18RD095	Gr	512788.5	7144020	13	67	356	16	130	4.558	1.022	-0.274
VT18RD096	Gr	512634.1	7143923	11	61	345	27	191	11.41	1.02	-0.185
VT18RD097A	Gr	512893.7	7143966	15	09	223	16	130	11.52	1.012	-0.205
VT18RD097B	Gr	512911.4	7143962	8	05	181	60	082	3.651	1.014	0.577
VT18RD098	Gr	512986.9	7143943	17	08	187	48	285	4.987	1.018	0.202
VT18RD099	Gr	512965.5	7143906	16	17	234	66	006	0.985	1.01	0.376
VT18RD100	Gr	512943.3	7144001	18	19	183	70	345	15.95	1.01	-0.444
VT18RD101	Gr	513018.3	7143979	11	20	223	57	346	0.836	1.009	-0.001
VT18RD102	Gr	512851.8	7144225	13	62	195	08	090	0.476	1.017	0.16
VT18RD103	Gr	512917.7	7143919	15	19	199	37	093	7.990	1.018	-0.562
VT18RD104A	Gr - Sh	513669.3	7144113	10	63	301	27	120	1.529	1.017	0.593
VT18RD104B	Gr - Sh	513669.5	7144114	11	36	230	24	121	4.139	1.044	0.703
VT18RD104C	Gr - Sh	513670.3	7144119	16	14	015	28	113	2.606	1.03	0.515
VT18RD105	Gr	513486.6	7144078	10	42	339	44	187	8.420	1.009	-0.137
VT18RD106	Gr	513162	7143974	17	38	257	36	023	3.800	1.004	-0.88
VT18RD107	Gr	513424	7144095	9	06	218	66	114	0.214	1.018	0.442
VT18RD108	Gr	513399.4	7144379	14	36	221	13	320	0.953	1.01	0.334
VT19RD01	Gr	510556.2	7147120	12	09	357	63	105	0.247	1.009	-0.456
VT19RD02	Ry	510487	7147147	7	41	193	25	307	38.90	1.088	0.815
VT19RD03	Gr	510886	7147424	8	02	357	71	260	19.38	1.018	0.065
VT19RD04	Nv	510659.1	7147542	16	03	346	60	080	27.39	1.067	-0.188
VT19RD05	Gr	512660.2	7144412	11	80	179	01	082	4.955	1.025	-0.27

Gr- Granodiorire/Granophyre; Ry – Rhyolite; Nv – Net-Vein Complex; Sh – Sample taken from inclined sheet

Table 1.